Fuel Cells: Optimizing Grain Boundaries in $BaZrO_3$ and Modeling Proton Conduction Using Kinetic Monte Carlo

A Thesis
Submitted to the Faculty
in partial fulfillment of the requirement for the degree of
Bachelor of Arts in Chemistry

by
Regina Ciszewski

Mount Holyoke College
South Hadley, Massachusetts
2012

I give permission for public access to my thesis for any copying to be done at the discretion of the archives librarian and/or the College librarian.

Regina Ciszewski

Date

Acknowledgements

I would like to thank everyone who helped to make this study possible. I am particularly indebted to my advisor, Maria Gomez, for all of the encouragement and guidance she provided me, and for all the wonderful opportunities I experienced while working with her. Thank you also to all of the members of the Gomez research group, for their continued support and encouragement throughout my thesis writing process and for fun times with balloon people on the research board.

I would also like to thank my family for their continued love and support. Your belief and confidence that I would succeed meant the world to me.

A special thank you to my other committee members, Margaret Robinson and Donald Cotter.

Finally I would like to thank my four amazing friends: Erica, Katie, Sam and Jeannie for keeping me sane with gifts of oranges.

Thank you also to the NSF for funding this project and the MERCURY Consortium for allowing me to use their wonderful computing resources.

Contents

1 Fundamentals of Fuel Cells **3**

1.1 Fuel Cells in Society 3

1.2 Fuel Cell Design and Mechanism 4

1.3 Different Fuel Cells 7

1.3.1 Alkaline Fuel Cells 7

1.3.2 Polymer Electrolyte Membrane Fuel Cells 8

1.3.3 Phosphoric Acid Fuel Cells 9

1.3.4 Molten Carbonate Fuel Cells 10

1.3.5 Solid Oxide Fuel Cells 11

1.4 Perovskite Oxides 13

1.5 Overview 17

2 Grain Boundaries and Optimization Tools **18**

2.1 Computational Methods 23

2.1.1 VASP 23

2.1.2 ReaxFF Reactive Force Field 24

2.2 Using Molecular Dynamics to Sample the Potential Energy Surface . . . 27
2.2.1 Molecular Dynamics . . . 27
2.2.2 Velocity Scaling . . . 31
2.2.3 Integrating Newton's Equation of Motion . . . 32
2.3 Results of Running Molecular Dynamics . . . 33
2.3.1 VASP Results . . . 33
2.3.2 ReaxFF Results . . . 38
2.4 Optimization with the Conjugate Gradient Method . . . 41
2.4.1 VASP Results . . . 41
2.4.2 ReaxFF Results . . . 44
2.4.3 Comparison of VASP vs. ReaxFF . . . 45

3 Octahedral Distortions and the Nudge Elastic Band Method 47
3.1 Octahedral Distortions of 23 Glazer Structures . . . 47
3.2 The Nudge Elastic Band Method . . . 52

4 Kinetic Monte Carlo Simulations of Proton Conduction Pathways 57
4.1 Kinetic Monte Carlo Method . . . 57
4.2 Graph Theory Methods . . . 63
4.3 Single Step Proton Pathways Through $BaZrO_3$ . . . 65
4.4 Multiple Step Proton Pathways Through $BaZrO_3$ . . . 70

5 Future Work **72**

List of Figures

1.1 Schematic for an individual fuel cell 5

1.2 SOFC schematic 12

1.3 General $BaZrO_3$ structure 14

1.4 Glazer Rotations 15

1.5 Basic proton movement 16

2.1 Tilt and twist grain boundaries 19

2.2 311 O-Terminated grain boundary 21

2.3 310 Zr-Terminated grain boundary 22

2.4 MD flow chart 30

2.5 Canonical MD energy in VASP 35

2.6 MD structure of 311 and 310 36

2.7 Micro-canonical MD energy 37

2.8 ReaxFF MD energies 38

2.9 ReaxFF MD equilibration energy 40

2.10 Optimized 311 O-Terminated system in VASP 42

2.11 Optimized 310 Zr-Terminated system in VASP 43

2.12 Optimized 311 O-Terminated system in ReaxFF 44
2.13 Optimized 310 Zr-Terminated system in ReaxFF 45

3.1 Atomic length of $BaZrO_3$ 48
3.2 NEB minimum energy pathway 52
3.3 NEB structures 53
3.4 Found minimum energy pathway 55

4.1 kMC electron in energy well 60
4.2 kMC method 62
4.3 RRTT pathway 66
4.4 RRTRRT pathway 67
4.5 RTRTRT pathway 68
4.6 RTTRTT pathway 69

List of Tables

1.1 Developed Fuel Cells and Their Characteristics 6

2.1 Converging Energy of NxNxN Unit Cells 26

3.1 Relative energies of 23 Glazer structures 51

4.1 Computational Time for N-step KMC 70

Abstract

Perovskite oxides have attracted much interest due to their possible use in proton conducting fuel cells. Today fuel cells have the potential to solve some of our nations most pressing problems, such as dependence on foreign oil, poor air quality, and greenhouse gas emissions that contribute to global warming. One of the critical limitations to proton conduction in fuel cells are defects in the conducting material. My research objective is to lay the foundation for proton conduction studies through grain boundaries by characterizing the structure of certain grain boundaries and developing a method that can model proton conduction through large systems containing grain boundaries. I focus on two types of defects, namely the O terminated (311) and Zr terminated (310) tilt grain boundaries in $BaZrO_3$. The specific grain boundary choices are motivated by earlier work which found the O terminated (311) surface to be of lower energy than others and one study on (310) tilt grain boundaries in $BaZrO_3$. The latter is the only calculation to date, which considered a specific grain boundary in $BaZrO_3$. Characterization of grain boundaries experimentally is very difficult and no studies have shown a successful characterization for grain boundaries in $BaZrO_3$.

Molecular dynamics on two approximate potential energy surfaces was used to sample a range of possible O terminated (311) and Zr terminated (310) tilt grain boundary configurations. Each sample point was optimized and the

lowest energy optimized structure was used to represent the relaxed grain boundary. The lowest energy grain boundary will be the basis for future work on proton conduction pathways through grain boundaries.

Since realistic grain boundary model systems are larger than model systems containing defects, I have also developed a new method to accelerate the simulation of proton conduction paths. The method uses graph theory pathways for small regions of the system to make multi-step moves in a traditional kinetic Monte Carlo (kMC) method. The net result is a longer-range motion for each step in the kMC dynamics. This method is tested on a $BaZrO_3$ perovskite system without grain boundaries where we have already found the proton conduction pathways.

Chapter 1

Fundamentals of Fuel Cells

1.1 Fuel Cells in Society

Sir William R. Grove first discovered the basic operating principle of fuel cells in 1839. To this day his principle remains unchanged: A fuel cell is an electrochemical device that is capable of transforming chemical energy directly into electric energy as long as fuel and an oxidant are supplied [1]. Unfortunately Grove's initial fuel cell experiment, which consisted of platinum electrodes placed in test tubes of hydrogen and oxygen, immersed in a bath of dilute sulphuric acid, was mechanically inefficient and caused significant corrosion of the electrodes. As a result, little scientific research on fuel cells followed for the next several decades. It wasn't until the beginning of the space race, in the late 1950's, that fuel cells were reconsidered, due to their light weight properties and high efficiency system.

Further fuel cell development is under investigation by a variety of electronics companies, power generating industries and automobile manufacturers. According to the United States Energy Information Administration, there is substantial uncertainty about the levels of future oil supply and demand. Furthermore, several states, such as California, have passed legislation calling upon auto manufacturers to produce zero emission vehicles, cars powered by electricity or alternative fuels rather than combustion engines. As a result, the push to create more fuel efficient vehicles has lead to the research and development of cars powered by fuel cells.

1.2 Fuel Cell Design and Mechanism

Fuel cells are comprised of three essential components: anode, cathode, and electrolyte as shown in Figure 1.1. Their basic design allows for the oxidation of fuel and reduction of oxygen. The oxygen and fuel are separated by an electrolyte that only ions (i.e. H^+, O^{2-}, ${CO_3}^{2-}$) can traverse. Two half-cell reactions occur at the anode and cathode electrodes. The character and stoichiometry of these reactions are determined by the molecular composition of the electrolyte [2].

Once the ions have traversed the electrolyte, oxygen will recombine in its reduced state with two protons to form water as a byproduct. The excess electrons are able to travel through an electrical wire, generating an electrical current to perform work. Since no direct combustion process occurs, fuel cells

are not limited by the theoretical Carnot efficiency, and have been calculated to operate at up to 50% efficiency.

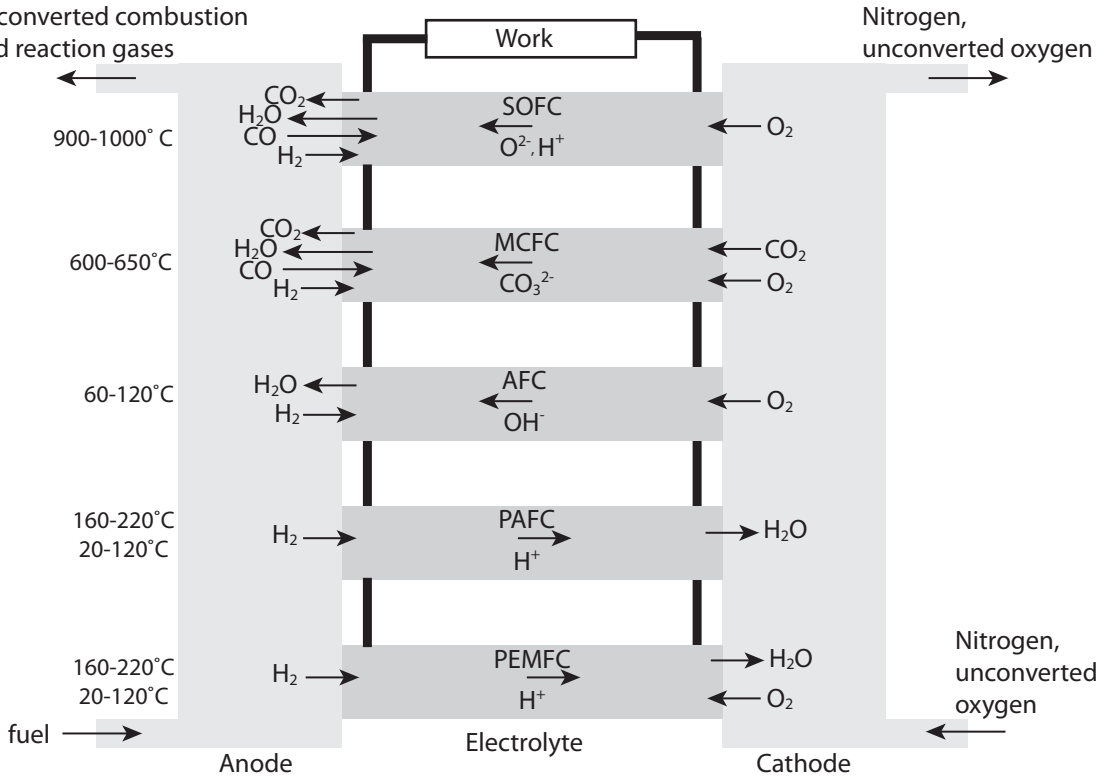

Figure 1.1: Schematic for a variety of fuel cells, which are all comprised of an anode, cathode and electrolyte. All five fuel cells shown have different optimum operating conditions. Based on the data in reference, Table 1.1 summarizes the mechanism of operation for each fuel cell.

Fuel cells are classified according to the type of electrolyte used for conduction. All good electrolytes must be leak tight, good ionic conductors and poor electron conductors, thin to reduce ionic resistance, and economically process-

able [2]. Similarly, a good electrode must be compatible with the electrolyte, have high electrical conductivity, high catalytic activity, and a large surface area [2].

In any fuel cell, the electrolyte is sandwiched between the anode and cathode. To reach the optimum reaction rate, the electrodes are flat to maximize contact area with the reactant and the electrolyte is thin to minimize resistance to the flow of ions. Often a platinum catalyst is added to the electrodes to speed up the rate of the reaction. The most common fuel cells and their standard characteristics are listed in Table 1.1 [1] and pictorially represented in Figure 1.1. The next sections discuss each fuel cell type in more detail.

Table 1.1: Developed Fuel Cells and Their Characteristics

Fuel Cell Type	Electrolyte	Charge Carrier	Operating Temperature	Fuel	Electric Efficiency
Alkaline FC (AFC)	KOH	OH^-	60-120°C	Pure H_2	35-55%
Proton Exchange Membrace FC (PEMFC)	Solid Polymer (i.e. Nafion)	H^+	50 - 100°C	Pure H_2	35-45%
Phosphoric acid FC (PAFC)	Phosphoric acid	H^+	220°C	Pure H_2	40%
Molten Carbonate FC (MCFC)	Lithium and potassium carbonate	$CO_3{}^{2-}$	650°C	H_2, CO, CH_4	>50%
Solid Oxide FC (SOFC)	Solid oxide electrolyte (yttria, zirconia)	O^{2-} H^+	1000°C	H_2, CO, CH_4	>50%

Fuel cells that operate at low temperatures, alkaline fuel cells and polymer electrolyte membrane fuel cells, are designed for mobile applications. Ceramic electrolyte and molten salt electrolyte fuel cells have a higher operating temperature and are designed for stationary applications [2]. More details on the merits of each fuel cell are discussed in the next section.

1.3 Different Fuel Cells

1.3.1 Alkaline Fuel Cells

Alkaline fuel cells (AFCs) were developed in the 1960's for use on the Apollo space missions [3]. The electrolyte used within AFCs in low concentration is potassium hydroxide. Within the fuel cell, oxygen is reduced at the cathode in the presence of water to form hydroxide, OH^-. The hydroxide ions then travel across the electrolyte towards the anode, where they react with hydrogen gas to form water. The half-cell and overall reactions are given by:

$$\text{Anode: } H_2 + 2OH^- \rightarrow 2H_2O + 2e^-$$
$$\text{Cathode: } \frac{1}{2}O_2 + H_2O + 2e^- \rightarrow 2OH^-$$
$$\text{Overall: } H_2 + \frac{1}{2}O_2 \rightarrow H_2O$$

Unfortunately, the conducting hydroxide ions are incredibly sensitive to the presence of CO_2 and will react with minute traces of the molecule. This reaction leads to carbon dioxide poisoning of the electrolyte and an overall decrease in the efficiency of AFCs. In order for AFCs to operate at an acceptable

efficiency CO_2 in the air would need to be removed. While this is possible, it lead to significant increases in the size and cost of the system [4]. Therefore most developers have turned their attention towards developing electrolytes which are non-alkaline.

1.3.2 Polymer Electrolyte Membrane Fuel Cells

Polymer electrolyte membrane, sometimes referred to as proton exchange membrane, fuel cells (PEMFCs) use solid polymer electrolytes. On either side of the electrolyte are porous carbon electrodes with a platinum catalyst, forming a membrane electrode assembly (MEA). At each electrode, the two half-cell reactions are given by:

$$\text{Anode: } H_2 \rightarrow 2H^+ + 2e^-$$
$$\text{Cathode: } \frac{1}{2}O_2 + 2e^- + 2H^+ \rightarrow H_2O$$
$$\text{Overall: } H_2 + \frac{1}{2}O_2 \rightarrow H_2O$$

At the anode, hydrogen gas bonds to the platinum catalyst, forming weak H-Pt bonds. Oxidation can occur as the hydrogen atoms recombine to release their electrons, which travel through an external wire to the cathode. Meanwhile, the protons must traverse across the polymer electrolyte. The most common PEM electrolyte material is Nafion, developed by DuPont in the 1970's [4]. The membrane polymer requires water to maintain the correct degree of hydration. The water in the membrane is responsible for transporting the proton by diffusion of hydrated protons as well as via proton transfer

between hydrated clusters [2]. Due to the need for a hydrated membrane PEMFCs operate at a relatively low temperature, around 50-100°C. At the cathode, the oxygen molecules similarly break apart and bond to the platinum catalyst, creating weak O-Pt bonds. Each oxygen will subsequently reform with two electrons and two protons to form water as the byproduct.

PEMFCs are currently at the forefront for use in automobile manufacturing. When they were first designed relatively large quantities of platinum were required. However recent developments in its use have ensured that the raw platinum material is now carefully deposited to ensure maximum surface area. With this new method of manufacturing it now costs as little as $10 for a 1-kW cell stack [2].

1.3.3 Phosphoric Acid Fuel Cells

Phosphoric acid fuel cells (PAFCs) contain an electrolyte composed primarily of phosphoric acid, H_3PO_4, a proton conductor. The half-cell reactions are the same as those for the PEMFC. PAFCs are utilized primarily for stationary applications and have been produced in both the U.S. and Japan [5]. The optimal operating temperature for the PAFC is between 150-200°C and is a compromise between electrolyte conductivity, which increases with temperature, and cell life, which decreases when temperature is increased [5]. However, the operating temperature provides design flexibility and allows PAFCs to be much less sensitive to carbon monoxide. Unfortunately the system still requires extensive fuel processing and requires expensive materials to produce. For these

reasons, over the past few years development of PAFCs have decreased in favor of PEMFCs.

1.3.4 Molten Carbonate Fuel Cells

Molten carbonate fuel cells (MCFCs) are a type of high temperature fuel cell that operate around 650°C. The electrolyte for this fuel cell is comprised mainly of salts such as lithium, sodium, and potassium carbonates [2]. Due to the high operational temperature, these salts melt and conduct the carbonate ions ($CO_3{}^{2-}$) from the anode to the cathode. At the anode, hydrogen reacts with a carbonate ion to produce water, electrons, and carbon dioxide.

$$\text{Anode: } H_2 + CO_3{}^{2-} \rightarrow H_2O + CO_2 + 2e^-$$

The electrons travel through a conduction wire to perform work, while the carbonate ion travels through the electrolyte towards the cathode. At the cathode, oxygen within the air reacts with carbon dioxide from the anode and two electrons to form water and carbonate ions.

$$\text{Cathode: } \frac{1}{2} + CO_2 + 2e^- \rightarrow CO_3{}^{2-}$$

The overall reaction taking place is given by:

$$\text{Overall: } H_2 + \frac{1}{2}O_2 \rightarrow H_2O$$

The main advantage of MCFCs is their ability to reform CO and certain hydrocarbons internally, limiting the formation of harmful waste products. Unfortunately the electrodes solubility within the electrolyte can lead to a

decrease in the surface area and a less effective fuel cell. Fixing this problem would require very expensive hardware to contain the corrosive electrolyte and the high operating temperature leads to material damage internally. Therefore, MCFCs have been developed primarily for stationary power generators because the liquid electrolyte is large and has a slow start-up time, making it unsuitable for mobile applications.

1.3.5 Solid Oxide Fuel Cells

Solid oxide fuel cells (SOFCs) have become some of the most efficient power generators. Due to their high operating temperature, they have applications in stationary and mobile generators. Researchers are investigating how SOFCs might be used for partial power supply in vehicles [4]. Since the operating temperature is so high (600-1000°C), the electrodes need to be made up of ceramic material. Typically, the anode is manufactured with $NiZrO_2$ or $CoZrO_2$ and the cathode with Sr-doped $LaMnO_3$ [6]. Similarly, the electrode is a solid, non-porous, ionically conducting ceramic. The two main types of electrolyte are fluorite structure and perovskite oxide structure [2]. The most common material used is yttria-stabilized zirconia (YSZ), doped lanthanum gallate ($LaGaO_3$), an oxygen ion conductor, and doped barium zirconate ($BaZrO_3$), a proton conductor. Figure 1.2 shows the schematic of a proton conducting SOFC. A more in-depth discussion on perovskite oxides can be found in the next section.

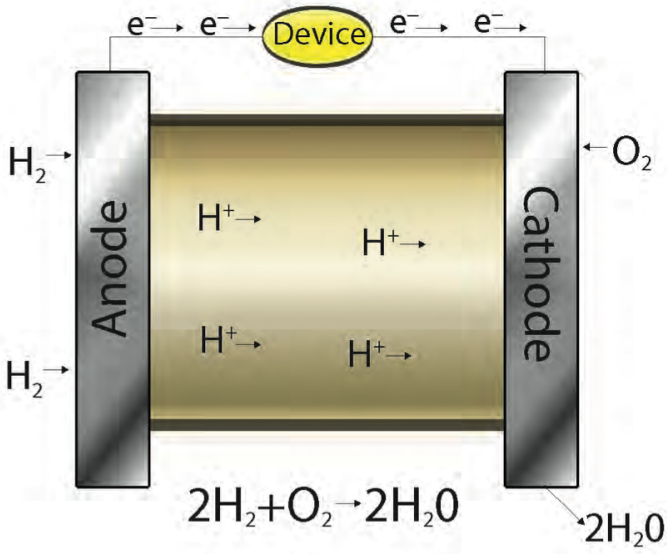

Figure 1.2: Schematic for a proton conducting SOFC comprised of a doped $BaZrO_3$ electrolyte, an anode and a cathode

The operational mechanism of a SOFC is straightforward. From an air flow along the porous cathode surface, the oxygen molecules are reduced. The resulting oxygen ions travel across the electrolyte towards the fuel rich anode. Once the oxygen ions encounter the fuel, either hydrogen or carbon monoxide, they react, producing water, carbon dioxide, heat, and electrons. The resulting electrons are able to travel through an external circuit, providing electrical energy. The half cell and overall reaction equations are given below:

$$\text{Anode: } H_2 + O^{2-} \rightarrow H_2O + 2e^-$$

$$\text{Cathode: } O_2 + 4e^- \rightarrow 2O^{2-}$$

$$\text{Overall: } H_2 + \frac{1}{2}O_2 \rightarrow H_2O$$

The main advantages to the solid structure of SOFCs is their lack of corrosion problems, and ability to avoid electrolyte movement or flooding of the electrodes [6]. The high operational temperature also allows for waste heat cogeneration or for heat use in bottoming cycles. Unfortunately, the high operating temperature needed for SOFCs also imposes restrictions on the type of materials used in the fabrication process which leads to increased manufacturing costs.

1.4 Perovskite Oxides

A perovskite oxide is a crystalline-like structure with the chemical formula ABO_3, where A and B denote two cations with different radii. The molecule A will usually have an oxidation number ranging from +1 to +3, and B will have an oxidation number between +3 to +6 [7]. Several examples of perovskite oxides include: $CaTiO_3$, $KTaO_3$, and $BaZrO_3$.

The ideal structure of a perovskite oxide is cubic. However, few compounds retain a perfectly cubic structure, and instead contain small distortions, leading the structure to be classified as orthorhombic, tetrahedral, or pseudo-cubic. The degree of distortion can be determined using the following equation:

$$t = \frac{R_A + R_O}{\sqrt{2}(R_B + R_O)} \tag{1.1}$$

where t is the tolerance factor, R_A is the ionic radius of A, R_B is the ionic

radius of B, and R_O is the ionic radius of oxygen. If the value of t is close to 1, the structure should display an ideal cubic or pseudo-cubic structure. When t is less than 1 the structure is orthorhombic, and t greater than 1 results in a tetrahedral structure. More information pertaining to the degree of distortion within perovskites will be discussed later in Chapter 3.

The calculations performed for this research were done using barium zirconium oxide, $BaZrO_3$. $BaZrO_3$ was predicted to be pseudo-cubic computationally [8], and several years later proven experimentally to be pseudo-cubic [9]. The structure of a single $BaZrO_3$ unit cell is given in Figure 1.3.

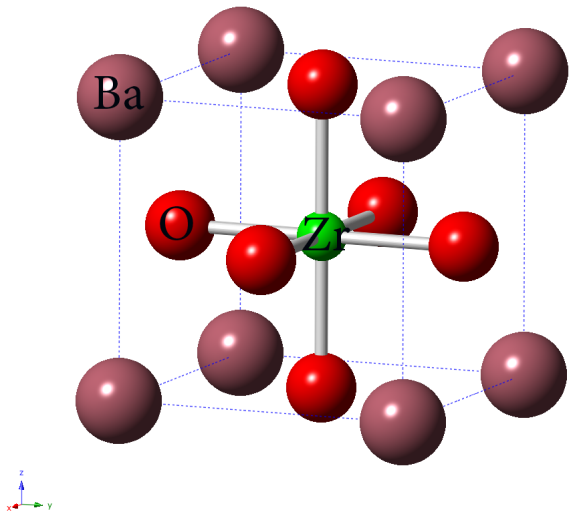

Figure 1.3: Structure of a single $BaZrO_3$ unit cell. The eight atoms located at each corner are barium, the central atom is zirconium, and the six atoms located at the center of each face of the cube are oxygen.

The structure of a single $BaZrO_3$ unit contains 5 atoms in its structure. In order to generate the cubic structure shown in Figure 1.3, the system is replicated outward in three dimensions. Due to replication outwards, the periodic boundary conditions stipulate that the left side of the cube generates the right side of the cube, with similar conditions for the top and bottom, and front and back of the cube.

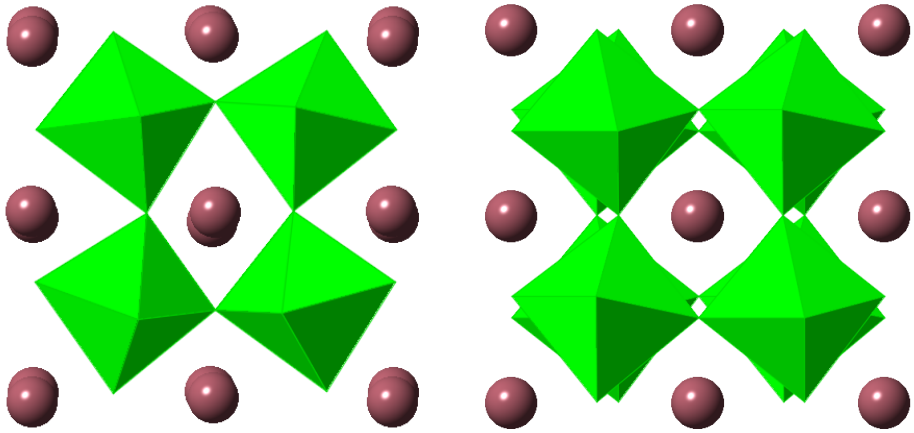

Figure 1.4: The perovskite $BaZrO_3$. The green octahedra have Zr cores. Different layers will rotate in (a) the same direction and (b) opposite directions

Perovskite systems that contain more than one unit cell will often display octahedral tilting between two layers. These layers can rotate in either the same or opposite directions, as shown in Figure 1.4. More on octahedral tilting will be discussed in Chapter 3.

Proton conduction pathways through $BaZrO_3$ are also considered. In experimental systems, the presence of a dopant is required to promote proton

conduction. Doping perovskites leads to a charge imbalance which can be filled by an oxygen atom from a water molecule [10]. The oxygen will then liberate a proton, which is free to conduct across the perovskite through a series of transfers and rotations from one oxygen to the next. The different types of movement available to a proton are shown in Figure 1.5. More information on locating and selecting proton conduction pathways will be discussed in Chapter 4.

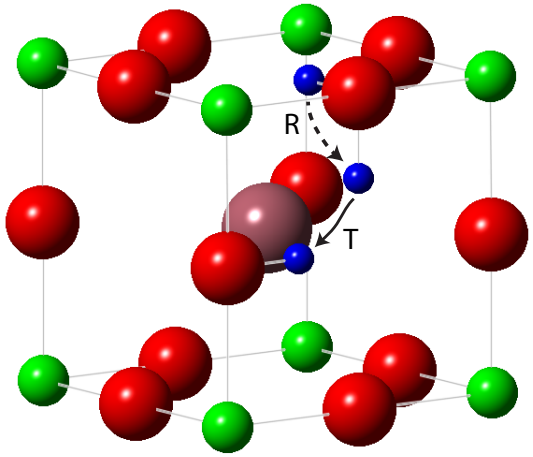

Figure 1.5: Two basic movements of the proton are possible: R and T. R, for rotation, is used when a proton rotates about the oxygen it is bound to. T, for transfer, is used when a proton moves to an adjacent oxygen within the same octahedron.

1.5 Overview

The goal of this work is to utilize kinetic Monte Carlo methods to select single and multiple-step pathways across the perovskite oxide $BaZrO_3$. To accomplish this goal, the grain boundary systems considered were first moved into a lower energy configuration using molecular dynamics (MD) and optimization techniques. Chapter 2 introduces the Vienna ab initio Simulation Package (VASP) and Reactive Force Field (ReaxFF), two separate programs used to find the energy of each $BaZrO_3$ system. Chapter 3 considers the cause of octahedral distortions within $BaZrO_3$ and the energy barrier that must be overcome in transitioning from one configuration to another. Chapter 4 describes the kinetic Monte Carlo and Graph Theory techniques used to find single and multiple-step pathways through $BaZrO_3$. Chapter 5 concludes with a discussion of what future research is still required, and what the project's next steps will entail.

Chapter 2

Grain Boundaries and Optimization Tools

The previous chapter highlighted the reaction mechanism and design of the most prominent fuel cells. Yet despite projections that fuel cell efficiency is capable of reaching and overcoming a 50% efficiency rate, a variety of challenges still limit the overall efficiency of the fuel cell. Just a few of the problems that must be overcome include, but are not limited to: the rate of transport of both the reactants to the electrolyte and desorption of the products away from the electrolyte, as well as the surface migration of the absorbed species across the electrolyte. The resistivity of the electrolyte plays a critical role in regulating the power density and work efficiency of the fuel cell [11]. Specifically, the formation of grain boundaries within the electrolyte is known to significantly slow down proton conduction.

A grain boundary results when two opposing crystals grow together at an interface, resulting in imperfections in the electrolyte's structure. At these grain boundaries, certain oxygen atoms are forced further apart, while others are moved closer together. Experimentally it has been observed that grain boundaries slow down conduction in perovskite oxides, while in other materials grain boundaries are known to increase the rate of proton conduction [12]. The properties and structure of a grain boundary are strongly influenced by impurity, sintering temperature, atmosphere and heat treatments [13].

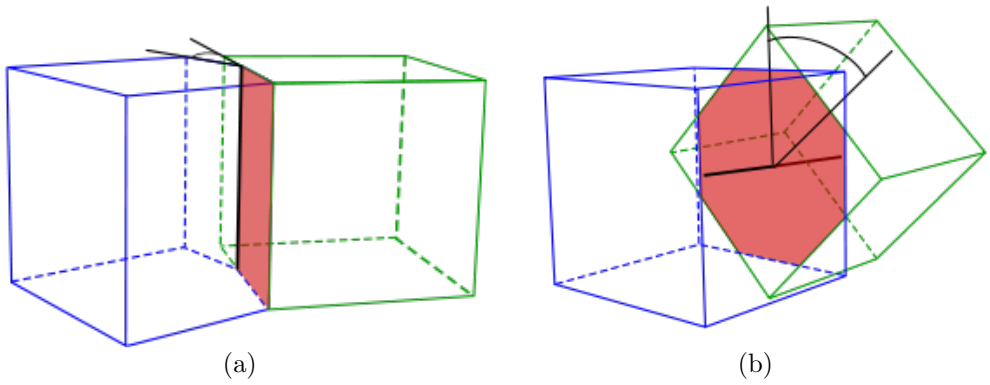

Figure 2.1: (a) Tilt grain boundary and (b) Twist grain boundary

Two possible grain boundaries can result within perovskite oxides, and are classified as either tilt or twist, as shown in Figure 2.1. The two grain boundaries considered for this paper are tilt 311 O-Terminated $BaZrO_3$ and tilt 310 Zr-Terminated $BaZrO_3$.

The surface classifications 311 and 310 are Miller indices. Written in general as (abc) in lowest terms, the values describe the lattice plane used to cut

the crystal. The general (abc) index defines a plane that intersects the x, y, and z axes at points $\left(\frac{1}{a}, 0, 0\right)$, $\left(0, \frac{1}{b}, 0\right)$, and $\left(0, 0, \frac{1}{c}\right)$. The lattice plane used to create the 311 O-Terminated and 310 Zr-Terminated surfaces are shown in Figure 2.2a and Figure 2.3a respectively.

To create a grain boundary, two cubic structures were cut with the same lattice plane. Then the two structures were brought together at a tilt to form a grain boundary. The specific grain boundary choices were motivated by earlier work which found the 311 O-Terminated surface to be of lower energy than others [14] and one study on 310 Zr-Terminated tilt grain boundaries in $BaZrO_3$. The latter is the only calculation to date, which considered a specific grain boundary in $BaZrO_3$ [15]. Figure 2.2b and Figure 2.3b show the grain boundary formation for the 311 O-Terminated and 310 Zr-Terminated surfaces respectively.

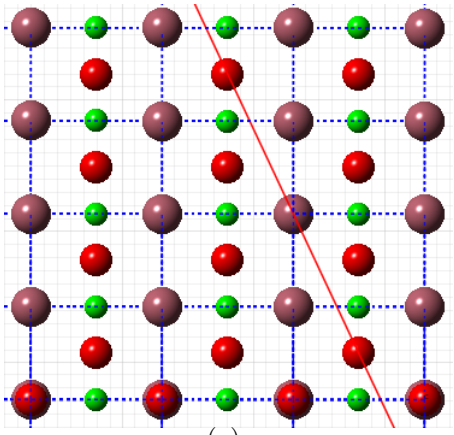

(a)

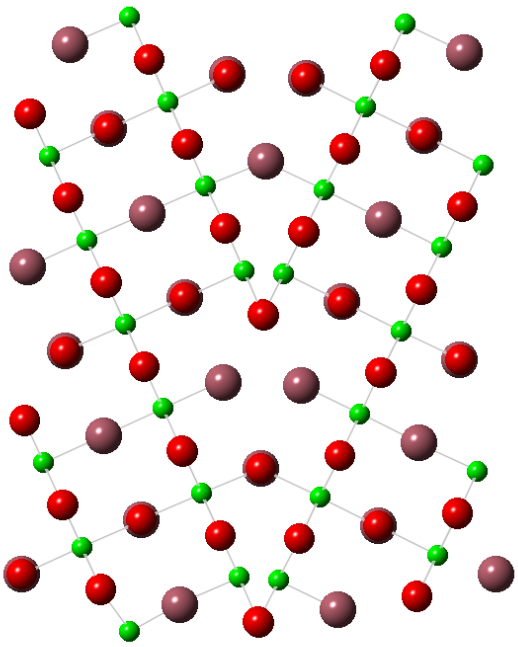

(b)

Figure 2.2: Pink, green, and red spheres are used to denote Ba, Zr, and O atoms respectively. (a) Planar view of a 3x4x3 $BaZrO_3$ unit cell. (b) Resulting 311 O-Terminated grain boundary

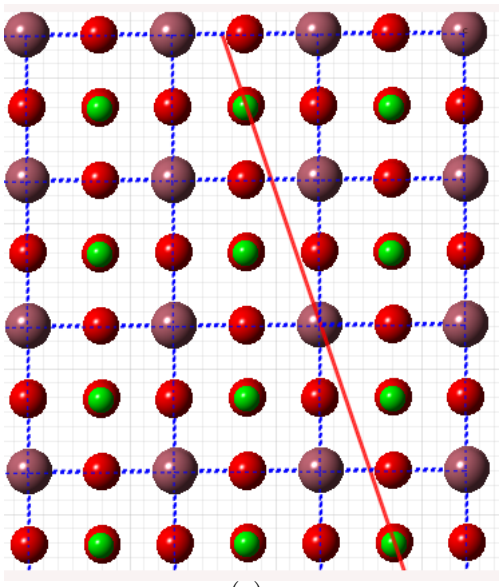

(a)

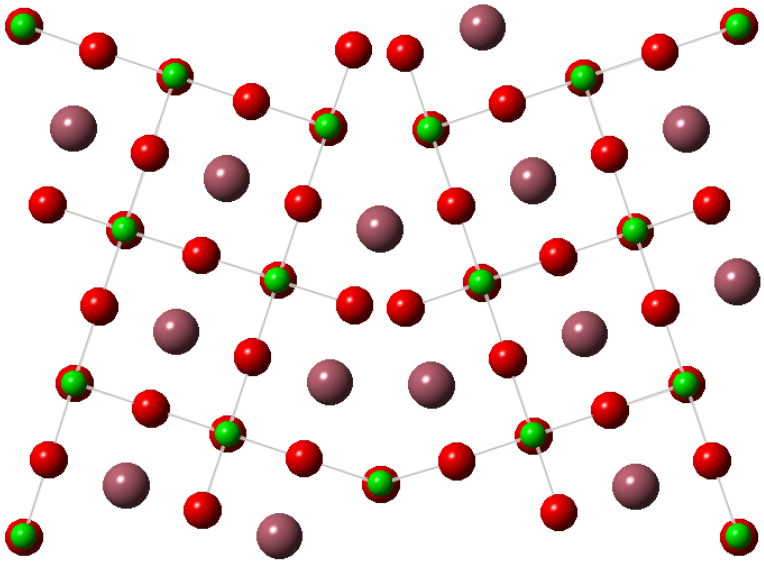

(b)

Figure 2.3: Pink, green, and red spheres are used to denote Ba, Zr, and O atoms respectively. (a) Planar view of a 3x3x3 $BaZrO_3$ unit cell. (b) Resulting 310 Zr-Terminated grain boundary

In order to calculate the energy of each grain boundary, the following equation was used:

$$E_{GrainBoundary} = \frac{E_{total} - nE_{unitcell}}{2A} \tag{2.1}$$

Here, E_{total} is the total energy of the grain boundary, $E_{unitcell}$ is the energy of a single unit cell, n is the number of unit cells, and A is the area of the grain boundary. To calculate the grain boundary energy, two different potential energy surfaces were used and are discussed in the following sections.

2.1 Computational Methods

In order to calculate grain boundary energies the Vienna ab initio Simulation Package (VASP) was used to find the lowest energy configurations. VASP is a versatile tool, developed by G. Kresse and co-workers [16], used to study the structural, dynamic and electronic properties of materials. Yet despite VASPs computational accuracy, the molecular dynamics and relaxation run times are costly, resulting in a search for a faster method. One possible solution is the Reactive Force Field (ReaxFF) method, developed by A. van Duin, W. A. Goddard and co-workers [17].

2.1.1 VASP

The Vienna ab initio Simulation Package (VASP) is a complex package used to perform ab initio quantum mechanical molecular dynamics and optimization.

To do this VASP uses the Born-Oppenheimer (B-O) approximation to solve the many bodied Schrödinger equation. Approximation techniques are required because the Schrödinger equation cannot be solved explicitly for any system more complicated than the hydrogen atom.

The B-O approximation allows the nuclei and electrons in the system to be treated separately. B-O fixes the distance between nuclei and allows their kinetic energy term to be ignored. The electronic portion of the Schrödinger equation is approximated using density functional theory (DFT) and the nuclei-electron interactions are described using pseudo potentials and the projector augmented wave (PAW) functions.

2.1.2 ReaxFF Reactive Force Field

Though the accuracy of modern quantum chemical techniques provides users with the ability to calculate geometries, energies, and vibrational energies to a precise amount, the simulation time required to compute these values for large scale systems is impractical. An alternative method is to employ force fields, which are based on potential energy functions, to accurately model the chemistry of molecules, resulting in a versatile computational tool. Reactive Force Field (ReaxFF) was initially developed by van Duin, Goddard and co-workers to study hydrocarbon systems in 2001 [18]. Since then ReaxFF has been adapted to fit a wide range of systems such as organic reactions [19], decomposition of improvised explosive devices [20], catalytic formation of carbon nanotubes [21], and many others.

ReaxFF makes use of a reactive force field, which is dependent on bond order terms when calculating potential energy. This is in contrast to non-reactive force fields which cannot simulate bond-breaking or bond-forming interactions. The systems potential energy for any molecule is described by

$$\begin{aligned} E_{system} = E_{bond} + E_{atom} + E_{lp} + E_{mol} + E_{val} + E_{coa} + E_{hbo} \\ + E_{tors} + E_{conj} + E_{vdw} + E_{coul} + E_{charge} \end{aligned} \tag{2.2}$$

Each energy term is used to describe either a bonded or non-bonded interaction within the system. The bonded terms taken into account are the bond energy (E_{bond}), the over and under coordination energy (E_{atom}), lone-pair energy (E_{lp}), molecular energy (E_{mol}), valence angle energy (E_{val}), angle conjugation energy (E_{cos}), hydrogen bond energy (E_{hbo}), torsion angle energy (E_{tors}), and energy of conjugation (E_{conj}). The remaining terms E_{vow}, E_{coul}, and E_{charge} describe the van der Waals, coulomb, and charge polarization energy for non-bonding interactions [17].

The ReaxFF potential energy is based largely on bond orders, which are obtained from interatomic distances and updated after every molecular dynamics or energy minimization step. Every bonded energy term is linked to bond order. This ensures that the energies and forces necessary will move toward zero as bonds dissociate [17]. Non-bonded interactions are also described between all atoms regardless of connectivity. In order to avoid excessive non-bonding interactions two parameters in the force field file are considered, the Upper Taper radius and the Cufoff for bond orders.

The Upper Taper radius describes the non-bonded cutoff radius and the Cutoff for bond orders describes the bond order threshold. These two parameters are used in conjunction such that if the distance between two atoms is less than the Cutoff the two atoms are considered bonded. Likewise, if the distance between the atoms is greater than the Upper Taper radius then the non-bonding interaction terms move toward zero.

The Upper Taper radius during out simulation was set at a distance of 10A, so any atoms farther than 10A apart are considered non-bonded and have no interaction term. However when energy minimizations were performed, several of the considered box sizes had lengths shorter than 10A. Due to periodic boundary conditions, when simulations are submitted, the original system is replicated outward in the x, y, and z direction. The result leads to the unrealistic scenario than an atom could interact with its own image. Table 2.1 shows the energy values calculated by ReaxFF for systems of 1x1x1, 2x2x2, 4x4x4, and 6x6x6 unit cells.

Table 2.1: Converging Energy of NxNxN Unit Cells

Simulation	Unit Cells	Box Size Length (Angstroms)	Total Energy (kcal/mol)	Energy/Unit Cell (kcal/mol)
1x1x1	1	4.26	-833.90	-833.90
2x2x2	8	8.52	-6672.65	-834.08
4x4x4	64	17.04	-53512.48	-836.13
6x6x6	216	25.56	-180581.51	-836.03

For the first two systems of 1x1x1 and 2x2x2 unit cells the decrease in energy per unit cell is only 0.2 kcal/mol. However when the system size in

increased to over 10A, the energy of the system decreases by 2.0 kcal/mol. It appears that the energy of a single unit cell is approaching -836.025 kcal/mol.

2.2 Using Molecular Dynamics to Sample the Potential Energy Surface

2.2.1 Molecular Dynamics

Molecular dynamics (MD) simulations provide researchers with the opportunity to view the time-dependent behavior of their system at an atomic level. In quantum mechanical MD, atoms are moved in discrete time steps by means of their integrated equations of motion. Using the classical time evolution of a particles initial position and velocity, the dynamics are derived from Newton's second law

$$a_i = \frac{d^2 r_i}{dt^2} = \frac{1}{m_i} F_i \tag{2.3}$$

where a_i is used to denote the acceleration of an electron i with mass m_i due to an instantaneous force F_i. It is assumed that $a = \frac{F_i}{m_i}$ is constant over the time interval Δt. However this is not actually the case, so our approximation will improve as the time step decreases. With appropriate forces, MD is capable of simulating particles traveling in space, colliding with one another, oscillating in concert, and evaporating from a free surface [22]. As a result of MD simulations, it is possible to calculate potential and kinetic energies of the system by averaging the trajectories of all electrons using statistical physics

[22].

A molecular dynamics simulation begins with atom initialization in which the coordinates of each atom are read in by VASP and placed in a periodic box system. Each atom is assigned an initial random velocity, such that the net momentum of the system is zero. The velocities of the atoms are scaled to bring the system to its desired temperature. More on velocity scaling is described in the next section.

After the initial conditions are set, the net force acing on each particle in the system is calculated. It is assumed that the total energy of the system is conserved

$$\frac{d}{dt}\left(\frac{1}{2}mv^2 + U(r)\right) = 0 \tag{2.4}$$

and the total force acting on a particle i is equal to the pairwise sum of forces between electron i and all other electrons $i \neq j$.

The forces acting on the electrons are derived from a potential energy function $U(r^N)$, where

$$r^N = (r_1, r_2, \ldots, r_N) \tag{2.5}$$

represents the complete set of $3N$ coordinates for all N electrons. Thus for every electron i, the force is given by

$$F_i = - \bigtriangledown_i U \tag{2.6}$$

Therefore, MD can be discussed in terms of either forces or potentials [22].

The interatomic potential is unique for each system it models. However

the accuracy of each potential is often a trade-off with computational resources. The potential function should include terms for each electron-electron, electron-nucleus, and nucleus-nucleus interaction within the system. In practice these calculations can be solved for only the most basic of systems, such as the hydrogen atom.

Once the forces on each atom are known, Newton's equation of motion is integrated to obtain the particles new position and velocity information. Details on the integration process are given in section 2.2.3. With the system now moved to a new orientation, the process can begin again until the simulation is complete. Figure 2.4 shows the general flow chart of the molecular dynamics algorithm.

Overall, molecular dynamics provides a method by which a large distribution of grain boundary structures can be sampled. This large sampling set will be needed when the structures are optimized. More on optimization techniques will be discussed in section 2.4.

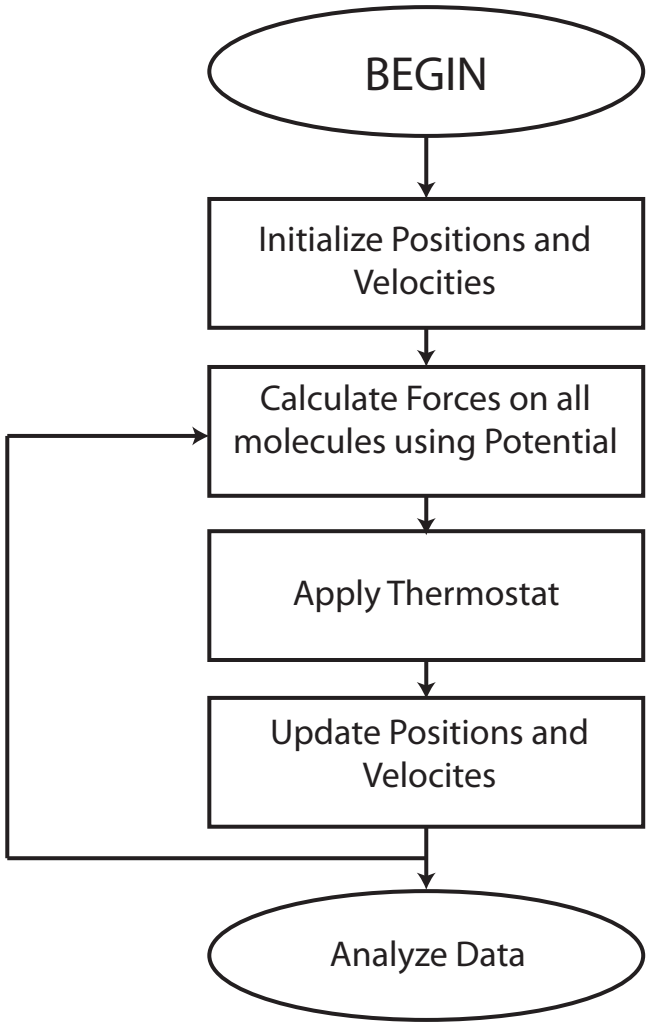

Figure 2.4: Flow chart schematic depicting the general molecular dynamics algorithm

2.2.2 Velocity Scaling

Initial systems usually contain poor geometrical configurations, resulting in an artificially high potential energy. As a result, beginning MD simulations are carried out allowing for scaling of velocities after every twenty steps. During the intermediate steps, the system is kept in a micro-canonical state, constant NVE. Switching to a canonical state, constant NVT, requires the presence of a velocity rescaling algorithm. Moreover, results produced by the ad hoc velocity rescaling algorithm are very reliable for a small enough time step [23]. To correlate temperature to velocity the equipartition of energy equation is used and given below

$$K.E. = \sum_{i}^{N} \frac{1}{2} m_i v_i = \frac{3}{2} N K_B T \tag{2.7}$$

where m_i is the mass of a single electron with velocity v_i. N is the total number of electrons in the system, k_B is Boltzman's constant, and T is the set temperature of the system. The electrons velocity will be rescaled to bring the system to the desired temperature using the equation below

$$v_i^{scaled} = \sqrt{\frac{T_{desired}}{T}} v_i \tag{2.8}$$

Notice that for velocity scaling, the equations of motion remain unchanged. Equation 2.7 is able to keep the kinetic energy of the system constant by multiplying all particle velocities by the same factor [24].

2.2.3 Integrating Newton's Equation of Motion

VASP is able to integrate Newton's equation of motion using the Verlet algorithm. Expanding the atoms position coordinates into the form of a third-order Taylor series, they are expressed in the form

$$r(t + \Delta t) = r(t) + v(t)\Delta(t) + \frac{1}{2}a(t)\Delta t^2 + \frac{1}{6}b(t)\Delta t^3 + O(\Delta t^4) \tag{2.9}$$

and

$$r(t - \Delta t) = r(t) - v(t)\Delta(t) + \frac{1}{2}a(t)\Delta t^2 - \frac{1}{6}b(t)\Delta t^3 + O(\Delta t^4) \tag{2.10}$$

so that the atoms positions are described in terms of forward and backward motion. Also, the variables v, a, and b are used to denote velocity, acceleration, and the third derivative of r with respect to t [16].

Adding Equations 2.9 and 2.10, the resulting position function is now defined as

$$r(t + \Delta t) = 2r(t) - r(t - \Delta t) + a(t)\Delta t^2 + O(\Delta t^4) \tag{2.11}$$

with an error propagation equivalent to Δt^4. Similarly, acceleration was defined previously in Equation 2.3 as force divided by mass, which is now written as

$$a(t) = -\frac{1}{m} \bigtriangledown U(r(t)) = \frac{d^2r}{dt^2} \tag{2.12}$$

Unfortunately, velocities are not generated directly by the Verlet algorithm. And while they are not needed for time evolution of the atoms, velocity is required to solve for the kinetic energy of the system. Also, to verify that the simulation is running correctly, the total energy of the system, E, calculated as $E = K.E. + U$, must be conserved as described in Equation 2.4.

To solve for velocity the atoms position coordinates are rewritten in the form of a first order taylor series, and then added together to produce

$$v(t) = \frac{r(t + \Delta t) - r(t - \Delta t)}{2\Delta t} \tag{2.13}$$

with an error propagation of Δt^2. While the Verlet algorithm produces reasonable results there are several other possible algorithms that have been shown to produce a smaller error associated with calculating new positions and velocities for atoms. One such methods is the leap-frog algorithm [25].

2.3 Results of Running Molecular Dynamics

2.3.1 VASP Results

Canonical MD was performed on the initial grain boundary of the 311 O-Terminated and 310 Zr-Terminated surfaces. Figure 2.5 shows a plot of each

surfaces' calculated energy for 2,000 time-steps. During the first two-hundred iterations both systems experienced a significant decrease in energy, confirming that the initial geometrical structure was unfavorable. After the first sharp energy drop both the 311 and 310 surfaces continued to decrease in energy, though at a significantly slower descent rate. Most importantly, by the final four-hundred iterations the energy of both systems had stopped decreasing, suggesting that both systems had settled into a favorable configuration allowing the atoms to move about in an equilibrated state. Figure 2.6 shows the final configuration of the 311 O-Terminated and 310 Zr-Terminated surfaces observed after 2,000 MD iterations.

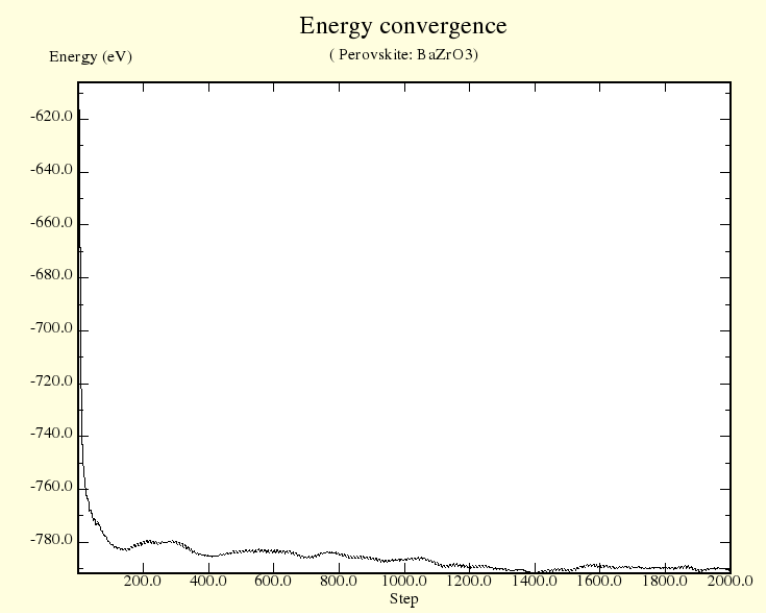

(a)

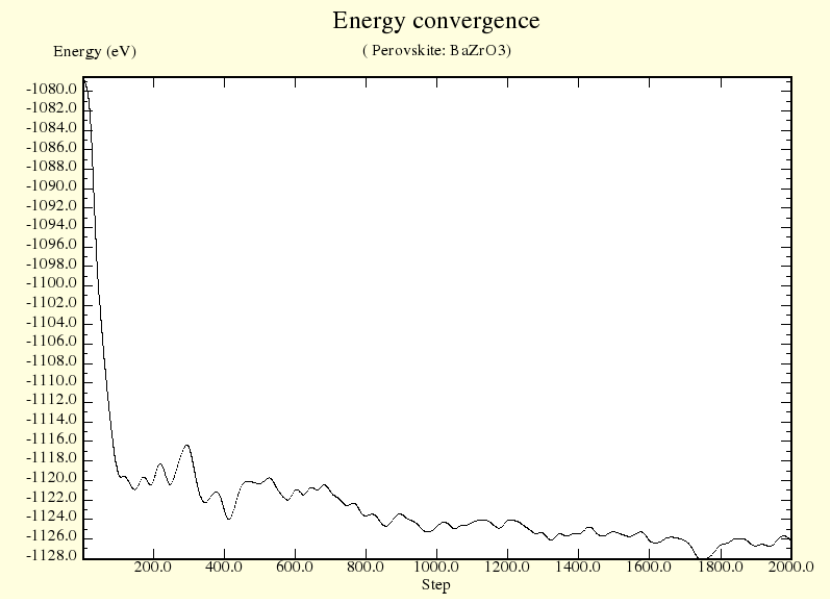

(b)

Figure 2.5: Grain boundary energy for 2000 MD steps in (a) 311 O-Terminated and (b) 310 Zr-Terminated surfaces

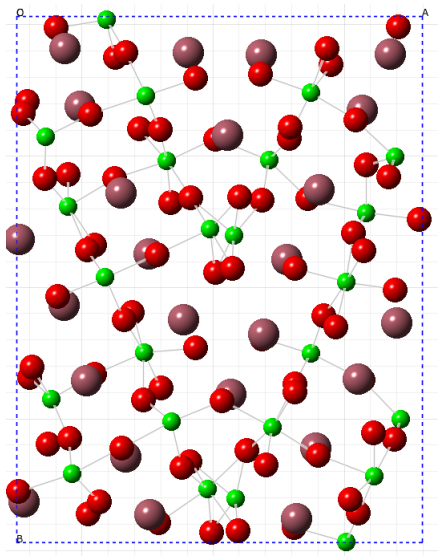

(a)

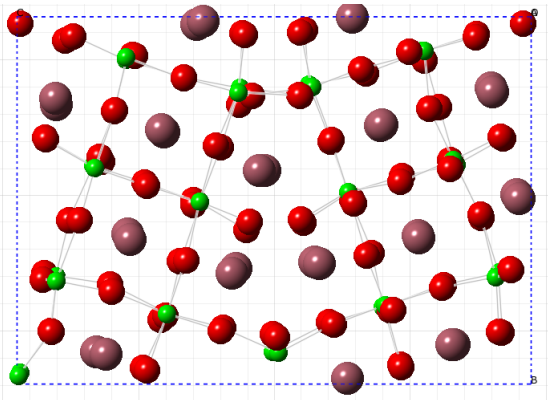

(b)

Figure 2.6: Resulting configuration of (a) 311 and (b) 310 after canonical MD

Since both systems had entered a stable state, the final configuration was captured to create two new initial structures and micro-canonical MD was performed for 2,000 more iterations. Figure 2.7 shows a plot of the resulting energies calculated for the 311 O-Terminated and 310 Zr-Terminated surfaces.

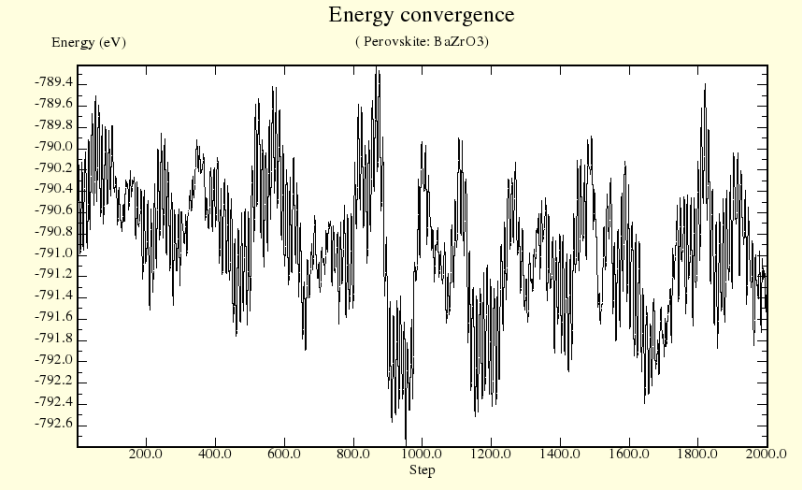

(a)

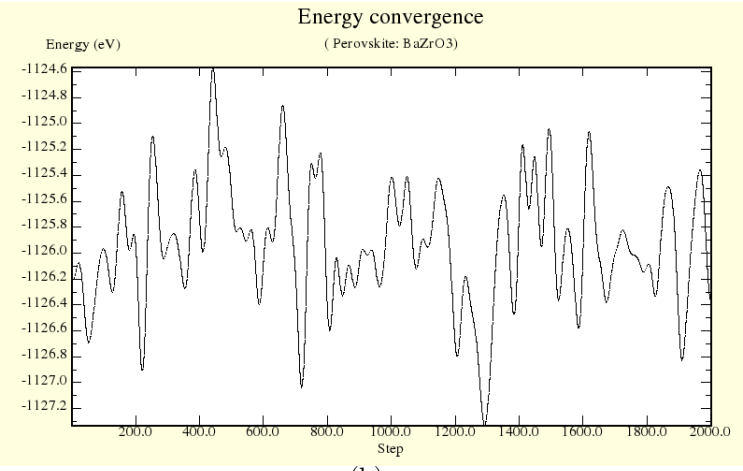

(b)

Figure 2.7: Grain Boundary energy of equilibration MD in (a) 311 and (b) 310 surfaces

System coordinates were printed out after every twenty iteration. The resulting one-hundred structures for each system acted as a random sampling of configurations that were subsequently optimized.

2.3.2 ReaxFF Results

The 311 O-Terminated and 310 Zr-Terminated grain boundary systems were allowed to run for 5,000 initial MD iterations. The resulting energies were printed out and shown in Figure 2.8.

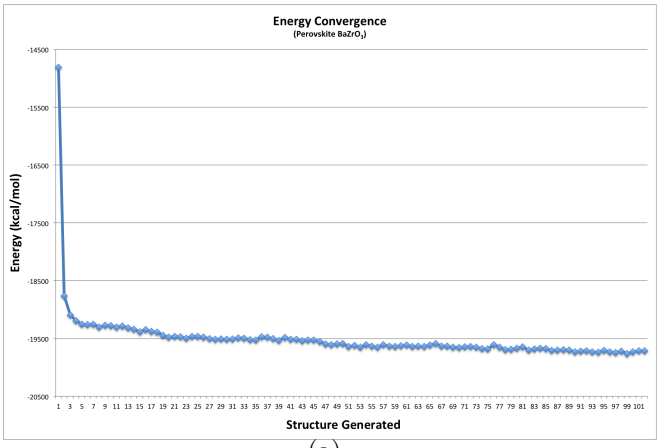

(a)

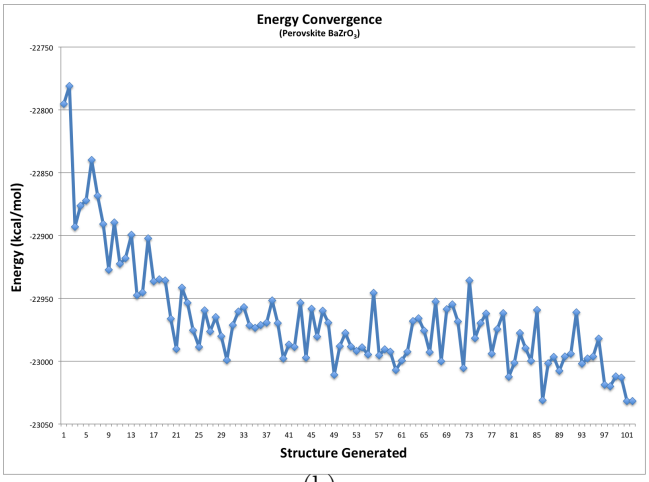

(b)

Figure 2.8: Grain Boundary energy for 5,000 steps in (a) 311 O-Terminated and (b) 310 Zr-Terminated surfaces

The shape of the graph in Figure 2.8a corresponding to the 311 surface is very similar to the type of activity observed in VASP. There is an initial steep decline in energy followed by a period of gradual decrease before equilibration is reached. However the graph in Figure 2.8b only displays the initial decline in energy. After 5,000 MD steps it does not appear that the system has reached equilibrium. Therefore the two systems were treated differently, during the second MD run. The 311 system was set to run for 10,000 MD iterations, while the 310 system was set to run for 50,000. Figure 2.9 shows a plot of the resulting energies.

System coordinates were printed out after every 100 iterations. The resulting 100 structures for the 311 O-Terminated system and 500 structures for the 310 Zr-Terminated system acted as a random sampling of possible configurations that were subsequently optimized.

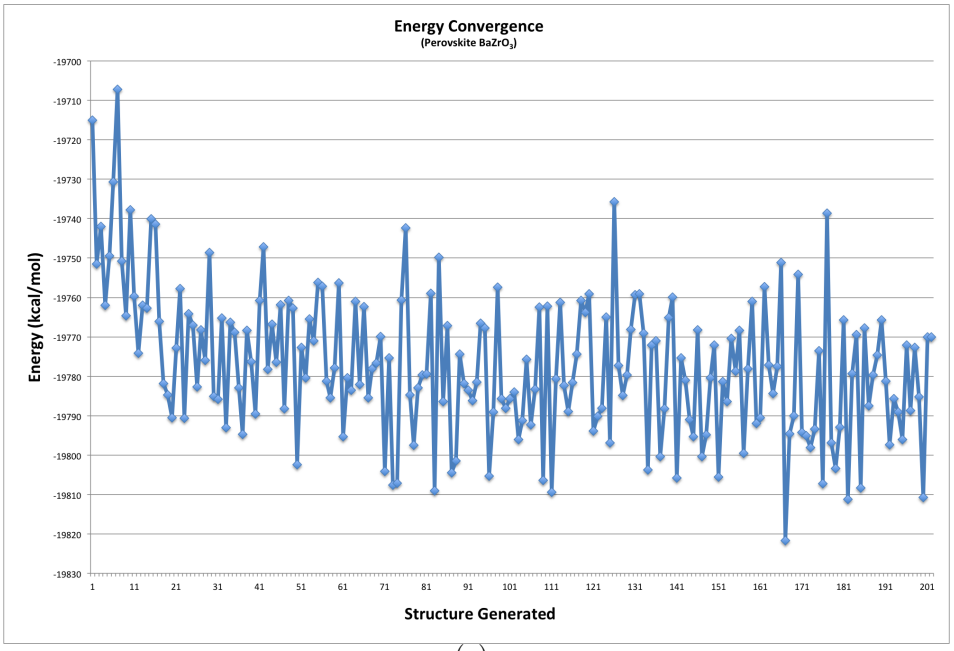

(a)

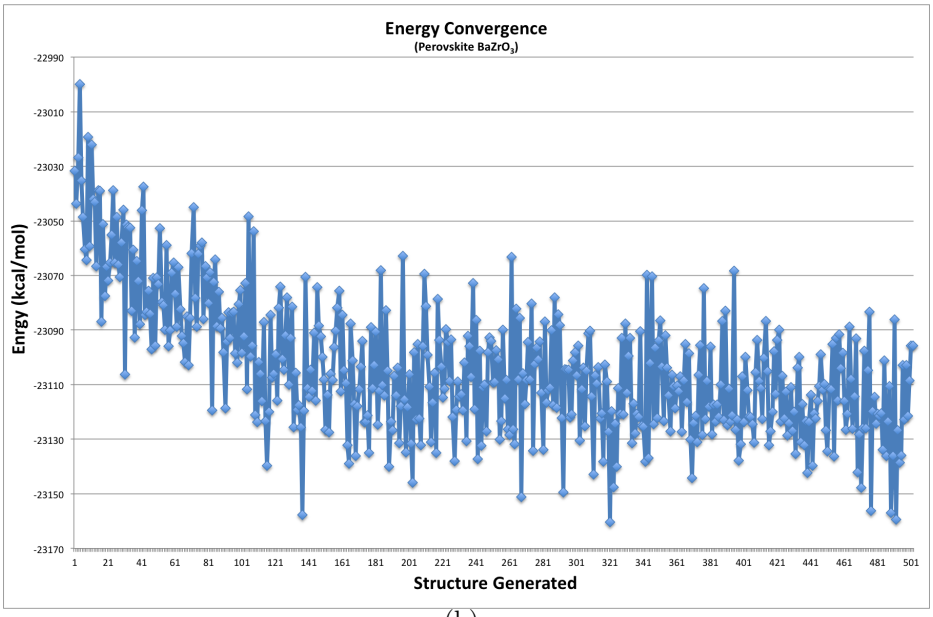

(b)

Figure 2.9: Grain Boundary energy for 5,000 steps in (a) 311 O-Terminated and (b) 310 Zr-Terminated surfaces

2.4 Optimization with the Conjugate Gradient Method

The conjugate gradient method (CG) method allows for the convergence of the atoms electronic configuration to their relaxed instantaneous ground state. The CG method requires a line minimization, which is calculated via a three step process [16]. First a trial step move is made towards the direction of greatest descent, then energies and forces are recalculated taking into account change in the total energy and total force. The process will repeat until a minimum is located. The minimum found will usually be a local energy minimum, there is no guarantee that the CG method will locate the global energy minimum of the system [26].

2.4.1 VASP Results

Each of the 100 randomly distributed structures produced from the 2,000 micro-canonical MD iterations were optimized in VASP using the conjugate gradient method. All 100 structures for the 311 O-Terminated system were successfully optimized into their corresponding minimum energy well. The energy of the grain boundary was subsequently calculated using Equation 2.1. The resulting energies displayed a large distribution, with the lowest 311 O-Terminated grain boundary energy calculated to be 0.12 eV and the highest energy was calculated at 1.45 eV. Such a large discrepancy in minimum energy values suggests that the potential energy surface has a variety of possible local

minima. The lowest energy configuration is shown in Figure 2.10.

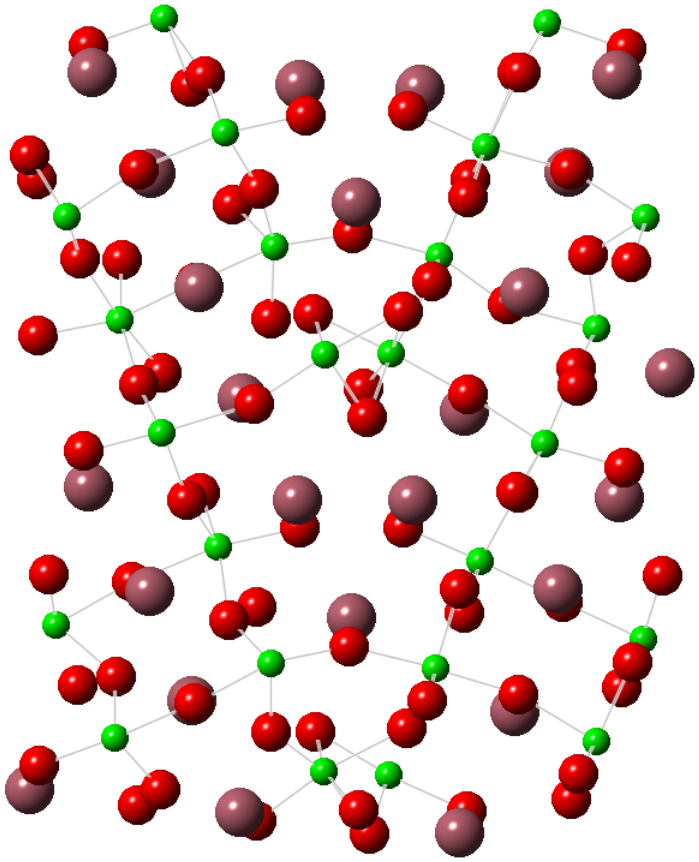

Figure 2.10: Minimum energy structure of 311 O-Terminated grain boundary, calculated to have an energy of 0.12 eV.

For the 310 Zr-Terminated grain boundary, 100 structures were set to optimize, but only 34 structures were able to finish running within the time constraints. For the structures that were optimized the energy of the grain boundary was calculated using Equation 2.1. The energy of all 34 310 Zr-

Terminated grain boundaries was calculated to be 0.11 eV. This value gives excellent agreement with the value of 0.10 eV calculated by Kim et al[15]. The lowest energy configuration is shown in Figure 2.11.

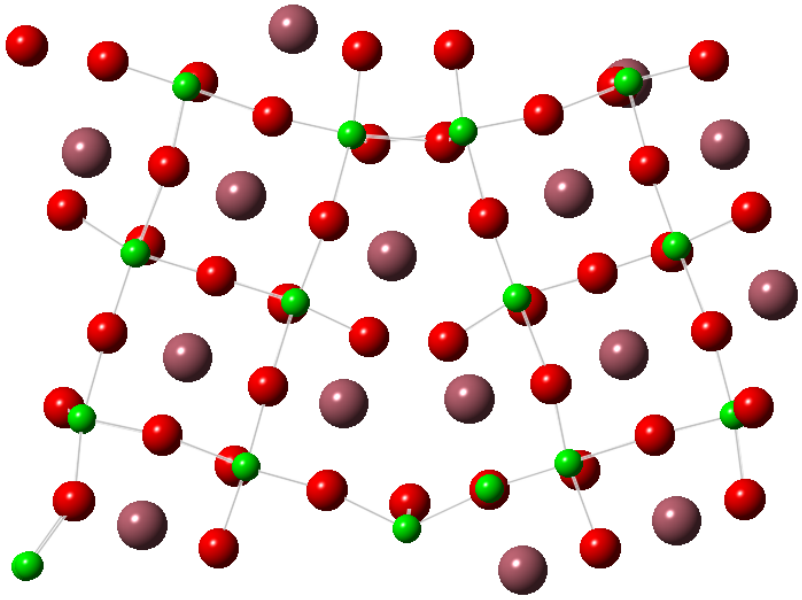

Figure 2.11: Minimum energy structure of 310 Zr-Terminated grain boundary, calculated to have an energy of 0.11 eV.

Thus far it appears that the potential energy surface of the 310 Zr-Terminated system is more uniform, allowing the majority of systems to move toward the global minimum instead of distributing systems into local minimum configurations. However a complete analysis will depend upon the energy of the remaining 66 structures.

2.4.2 ReaxFF Results

Each of the 100 generated 311 O-Terminated systems were successfully optimized in ReaxFF, and their grain boundary energies were calculated using Equation 2.1. The highest grain energy calculated was 0.02 eV and the lowest grain boundary energy calculated was 0.01 eV. The lowest energy structure is shown in Figure 2.12.

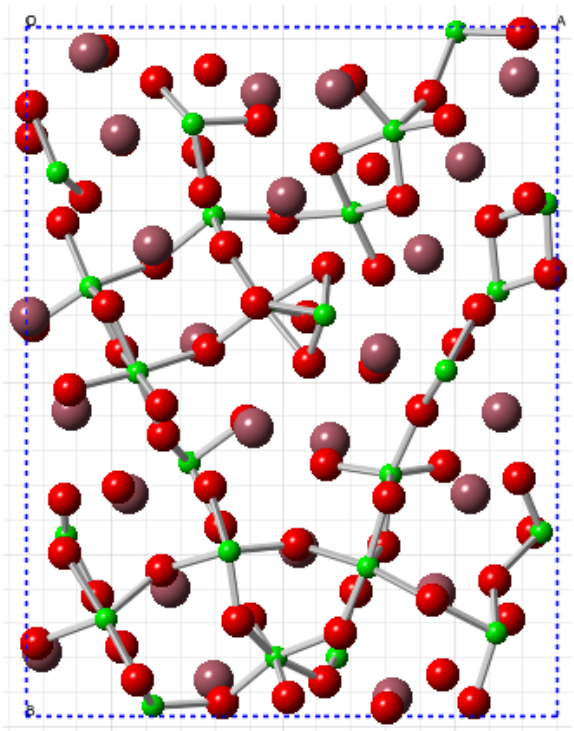

Figure 2.12: Minimum energy structure of 311 O-Terminated grain boundary, calculated to have an energy of 0.01 eV.

Similarly, the 500 generated 310 Zr-Terminated systems were optimized

and their grain boundary energies were calculated using Equation 2.1. The highest grain boundary energy calculated was 0.03 eV and the lowest grain boundary energy calculated was 0.02 eV. The lowest energy structure is shown in Figure 2.13.

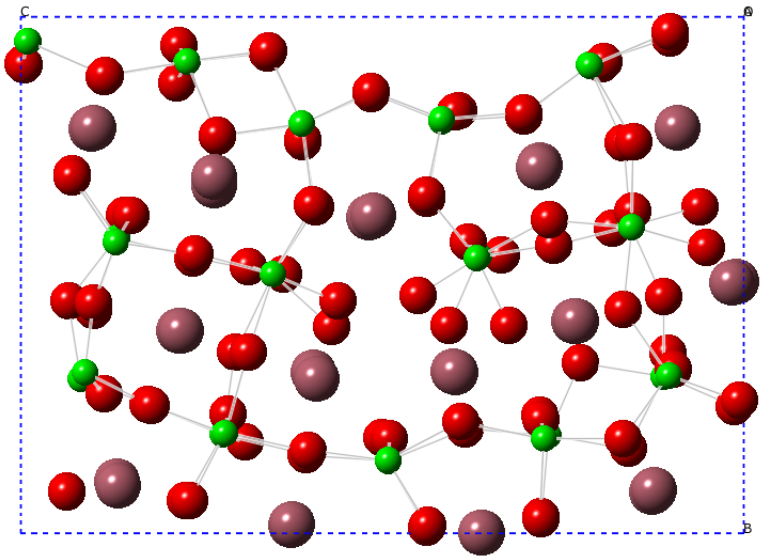

Figure 2.13: Minimum energy structure of 310 Zr-Terminated grain boundary, calculated to have an energy of 0.02 eV.

2.4.3 Comparison of VASP vs. ReaxFF

For MD iterations, both structures displayed the same general trends of a sharp decline in energy followed by a gradual decline as equilibrium was attained. Yet for structures run in VASP calculations and run time were longer, but a smaller number of MD iterations were required to reach equilibrium. While

ReaxFF ran faster, reaching equilibrium required up to 50,000 MD steps.

For optimization, it was previously noted that the final energies calculated by VASP showed a much better agreement with previous results. However ReaxFF reports results that are significantly lower in energy. In addition, the two programs differ on the extend to which atoms are reconfigured in their lowest energy structure. VASP was much more reserved at shifting atom positions and as a result the grain boundary remains largely intact. On the other hand, the resulting structures minimized by ReaxFF displayed a larger distribution of atom movement from their initial positions. However it is interesting that the more distorted ReaxFF structures are lower in energy. It is possible, with the greater distortions that ReaxFF is attempting to shift the systems toward a different grain boundary configuration that is lower in energy.

Chapter 3

Octahedral Distortions and the Nudge Elastic Band Method

3.1 Octahedral Distortions of 23 Glazer Structures

Perovskite oxides were first discussed in Chapter 1 Section 4. Equation 1.1 is used to predict what type of distortions a system will display based on the radius of certain atoms. Consider a general perovskite oxide that is perfectly cubic with sides of length a_0. Then the height of the box can be described as

$$a_0 = 2(r_B + r_O) \tag{3.1}$$

Similarly, the diagonal across one face of the cube can be described math-

ematically by

$$\sqrt{2}a_0 = \sqrt{a_0^2 + a_0^2} \tag{3.2}$$

Or the length of the box can be defined in terms of the atoms along the diagonal as

$$a_0 = \frac{2}{\sqrt{2}}(r_A + r_O) \tag{3.3}$$

Figure 3.1 depicts the length of the perovskite in terms of the radius of the atoms.

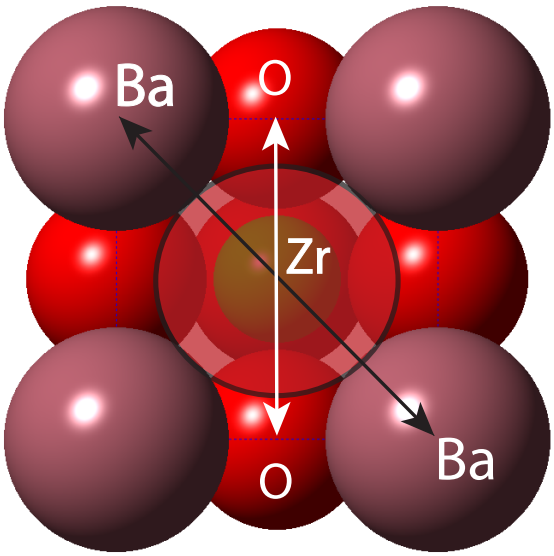

Figure 3.1: Length of $BaZrO_3$ in terms of atoms along the center (0-Zr-0), and atoms along the diagonal (Ba-O-Ba).

With two expressions for the length of the box, their ratio is considered and simplified to

$$1 = \frac{a_0}{a_0} = \frac{\frac{2}{\sqrt{2}}(r_A + r_O)}{2(r_B + r_O)} = \frac{(r_A + r_O)}{\sqrt{2}(r_B + r_O)} \tag{3.4}$$

which can also be thought of as

$$(r_A + r_O) = \sqrt{2}(r_B + r_O) \tag{3.5}$$

However as atom A's radius decreases, a point will be reached when the cation is too small to remain in contact with the oxygen atoms within the system. At this point, the B-O-B bonds are forced to bend, tilting the structure and bringing atom A back into contact with oxygen. To account for this distortion, the tolerance factor t is introduced into equation 3.5.

$$t = \frac{(r_A + r_O)}{\sqrt{2}(r_B + r_O)} \tag{3.6}$$

Consider the case where the radius of atom A decreases, or the radius of atom B increases, then the tolerance factor will be associated with a value less than 1 ($t < 1$). The overall structure will distort to favor an orthorhombic structure. In the case where the radius of atom A increases, or the radius of atom B decreases then the tolerance factor will increase to values greater than 1 ($t > 1$), and the perovskite structure will favor an octahedral or tetrahedral structure.

As a result of the tilting described, it is possible for different layers of a perovskite to distort into a variety of configurations. Glazer [27] identified 23 possible octahedral distortions that occur in a $2x2x2$ perovskite. Distortions along the x, y, and z axes are considered and labeled according the Glazer's notation. Two layers that rotate in the same direction are denoted as (+), while two layers that rotate in the opposite direction are denoted as (-). If no distortion occurs the system is denoted with (0).

The 23 structures each contained 8 Ba, 8 Zr, and 24 O atoms, a $2x2x2$ unit cell. Structures were optimized using VASP and ReaxFF. The resulting energies and final configurations are given in Table 3.1.

After minimization, the lowest energy structures found were #12 with a (- - -) structure in VASP and # 20 with a (0 - -) structure in ReaxFF. Both programs identified #23, with a perfect cubic (0 0 0) structure, as the highest energy configuration. The next two lowest structures found with VASP were # 13 and # 14, both of which had been minimized to the (- - -) configuration. ReaxFF on the other hand found # 14 and # 12 to be the next lowest in energy, yet both had configurations of (- - -). VASP calculated the energies of the structures to be more tightly clustered together than ReaxFF, which saw a larger range of energies attained. The difference in energy between the highest and lowest structure was 0.03 eV in VASP, but 4.0 eV in ReaxFF. The VASP structures never experienced a deviation from their initial configurations, while ReaxFF structures experienced more distortions, but the majority still retained their initial configurations. The lowest energy structures were

compared, and it was observed that minimization with VASP resulted in fewer physical distortions than the structures minimized with ReaxFF experienced.

Table 3.1: Relative energies for the 23 Glazer structures, optimized using VASP and ReaxFF. The notation 0/- is used to describe tilting to a lesser extent than a complete (-).

Structure	Initial Structure.	VASP (eV)	VASP Structure	ReaxFF (eV)	ReaxFF Structure
1	+++	0.04	+++	0.62	+++
2	+++	0.04	+++	0.62	+++
3	+++	0.03	+++	0.46	+++
4	++-	0.02	++-	0.78	0+-
5	++-	0.02	++-	0.76	++-
6	++-	0.02	++-	0.38	0 + -
7	++-	0.02	++-	0.77	++ -
8	-+-	0.01	-+-	0.39	0- -
9	-+-	0.01	-+-	0.42	0/- - -
10	-+-	0.01	-+-	0.37	+ 0/- -
11	-+-	0.01	-+-	0.40	+ - -
12	- - -	0.00	- - -	0.20	- - -
13	- - -	0.00	- - -	0.29	- - -
14	- - -	0.00	- - -	0.18	- - -
15	+0+	0.04	+0+	0.62	0++
16	+0+	0.03	+0+	0.61	0++
17	+0-	0.02	+0-	0.52	0 +-
18	+0-	0.02	+0-	0.48	0 + -
19	0- -	0.01	0 - -	0.57	0 - -
20	0- -	0.01	0 - -	0	0 - -
21	00+	0.04	00+	0.77	00+
22	00-	0.02	00-	0.92	00-
23	000	0.04	000	3.96	000

3.2 The Nudge Elastic Band Method

The transition state between the highest, # 23, and lowest, #14, energy Glazer structures is considered. The nudge elastic band (NEB) method is used to optimize the transition state and locate a minimum energy pathway (MEP) between the initial and final states. To begin a plot of the energy vs. reaction coordinate is constructed, and shown in Figure 3.2.

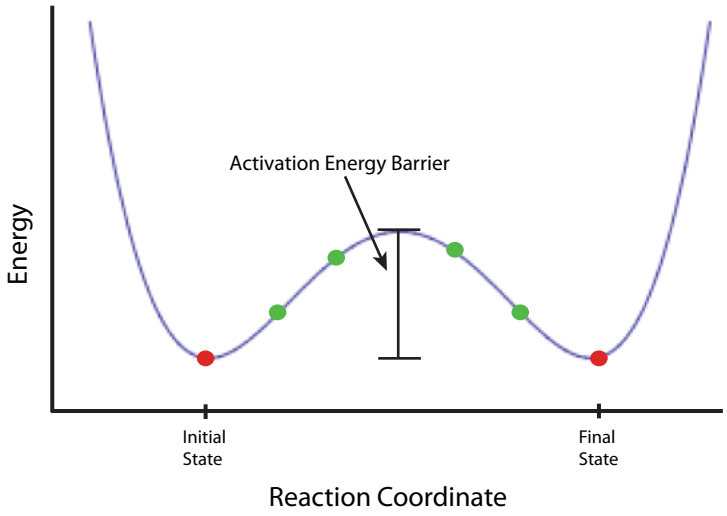

Figure 3.2: Plot of the minimum energy pathway

Next a set of 4 intermediate images are generated between the final and initial states, Figure 3.3 shows the six sites considered. These N+1 states can be denoted as

$$[R_0, R_1, R_2, \ldots R_N] \tag{3.7}$$

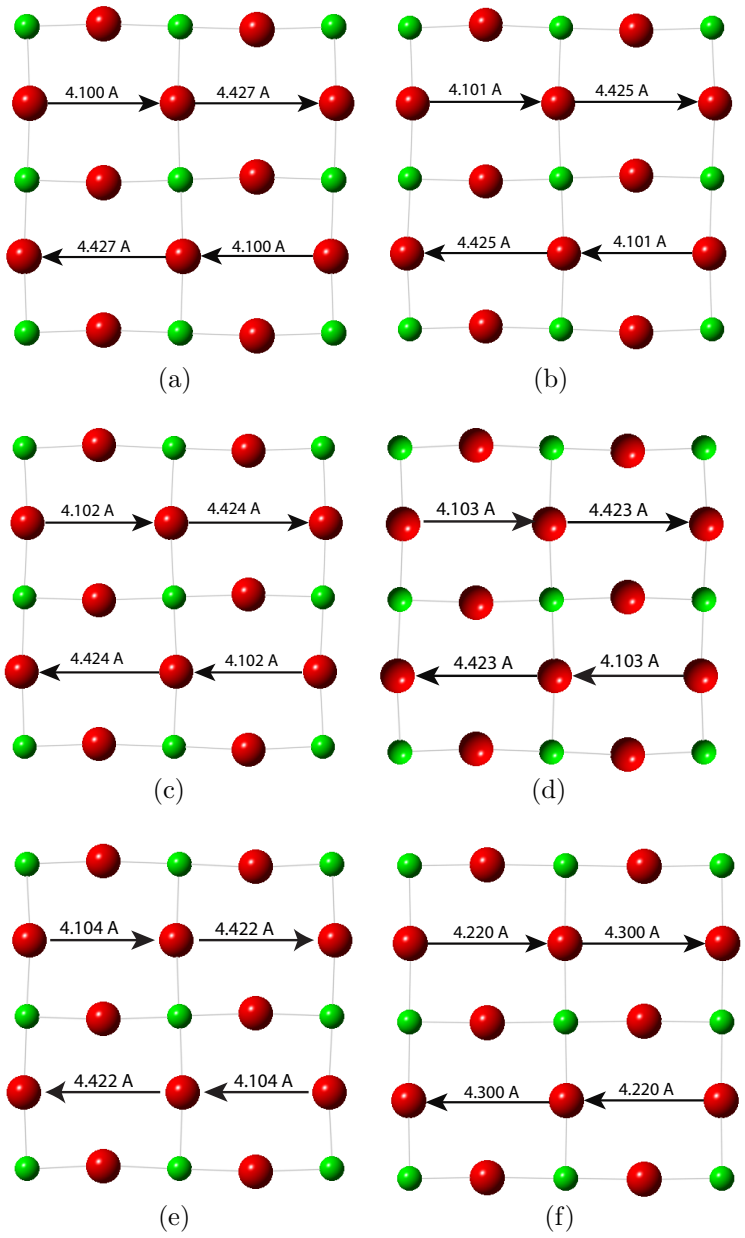

Figure 3.3: Measured changes in the distance between opposing oxygen atoms. (a) Initial state (- - -). (b-e) Intermediate images. (f) Final state (0 0 0).

Spring forces, acting like elastic bands, are required to control the spacing between the images. A converged path depends heavily on the choice of the spring constant, k, and should be chosen on the same order as the force constants for efficient optimization [28]. Otherwise the forces acting on the path cause the images to slide down from the higher energy regions towards the minimum, this is known as the "sliding down" problem. The total NEB force acting on a single image i is the sum of the spring force along the local tangent and the true force perpendicular to the local tangent. These forces are expressed as:

$$F_i^{NEB} = F_i^{s\parallel} + F_i^{\nabla\perp} \tag{3.8}$$

where $F_i^{\nabla\perp}$ is the potential force due to the gradient which contains parallel and perpendicular components and $F_i^{s\parallel}$ is the spring force parallel to the path. The spring force is written formally as

$$F_i^{s\parallel} = k(|R_{i+1} - R_i| - |R_i - R_{i-1}|) \tag{3.9}$$

An optimization algorithm is then used to move the images according to the forces in Equation 3.8. The MEP found will contain a maximum that corresponds to a saddle point on the potential energy surface. Unfortunately the resolution along the MEP is poor near the saddle point and the activation energy is subject to large uncertainty [29].

Therefore, climbing NEB (cNEB) is utilized, such that the highest image

will converge to the saddle point along the path [28]. Once the highest energy image on the MEP is identified, it is optimized alone. The only force now acting on the image is the inverted potential, causing the image to move up the potential energy surface [29]. Because no spring constants are considered during cNEB, the barrier located is significantly more accurate. Figure 3.4 illustrates the different saddle points and MEP found when using NEB and cNEB methods.

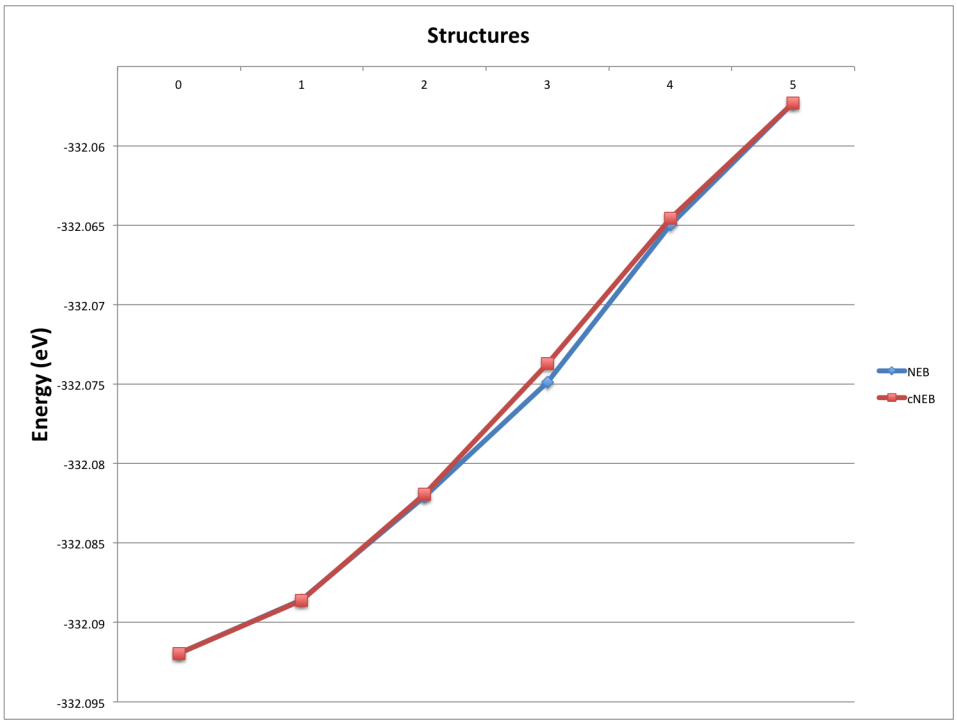

Figure 3.4: The MEP pathways located using regular NEB (blue line) and cNEB (red line)

For this particular transition, the NEB and cNEB failed to identify the true energy barrier. Due to the extremely unfavorable 05 configuration, the

activation energy is minute and therefore lies closer to the higher energy structure, making intermediate structure sampling difficult. Typically intermediate structures will lie on both sides of the barrier, however in this situation all 4 structures lie to the left of the barrier. The length of segment to the right of the barrier is so small that a larger number of intermediate images will need to be generated for an accurate calculation of the transition state energy.

Chapter 4

Kinetic Monte Carlo Simulations of Proton Conduction Pathways

4.1 Kinetic Monte Carlo Method

The Monte Carlo method, developed during the 1940s at Los Alamos National Laboratory, involves games of chance whose outcome is used to study some intriguing event [30]. In general, Monte Carlo (MC) refers to a broad class of mathematical algorithms that are solved with help from random number generators. To date there have been several variations on classic Monte Carlo methods such as: Metropolis Monte Carlo and kinetic Monte Carlo. Due to the flexibility of these algorithms, the MC method is useful in an extremely

wide range of applications, from simulating radiation damage annealing to the formation of galaxy clusters [31]. The focus of this paper is kinetic Monte Carlo (kMC) and the processes it utilizes to evaluate the dynamical evolution of a system.

Development of the kinetic Monte Carlo (kMC) algorithm began in the early 1960s and was designed for evolving systems dynamically from state to state [32]. Before kMC, simulations of pathways were considered using molecule dynamics (MD) requiring Newton's classical equations of motion to analyze the movement of atoms within the system. The resulting development produced excellent agreement with the physical system, however the total simulation time was unable to run for time-scales longer than one microsecond due to the necessity of solving and resolving for atomic vibrational states. Consequently, many processes, such as the effects of a cascade event, were unable to be properly evaluated due to this time-scale problem.

In an attempt to overcome the time-scale problem the kMC method utilizes the fact that long time dynamics consists mainly of jumps from one state to another with long periods of relative inactivity between these states. This approximation allows for the smaller time steps to be condensed into larger-scale processes that encompass the collective action of many sub-processes [31]. kMC is thereby able to treat state-to-state transitions directly, eliminating the need to recalculate intermediate vibrational modes [32]. This adaptation to the program allows kMC to reach increasingly larger time scales spanning several microseconds to several seconds.

It is relatively simple to visualize what is occurring at the molecular level and how this translates into a kMC mathematical algorithm. Imagine a perfect periodic boundary condition system that has been energetically minimized into its corresponding energy well. The system, which is currently in state i, is able to vibrate within its minimum energy well. Surrounding state i are other potential energy wells, which are separated by an energy barrier. When given sufficient energy, state i can cross any one energy barrier, moving the system from state i with geometric configuration G_i to state j with a new geometric configuration G_j. Figure 4.1 depicts a proton vibrating within a minimum energy well.

For each possible escape route there is a corresponding rate constant k_{ij}, which depicts the probability per unit time that state i escapes to state j. It is important to note that the system does not remember previous moves, therefore the rate constant k_{ij} does not depend on any preceding configurations, but is instead determined by the shape of the potential basin i, the shape of the ridge-top connecting i to j, and the shape of the potential basin j [32]. The more favorable the reaction, the larger the rate constant k_{ij} will be.

Each adjacent system bordering state i corresponds to a unique rate constant k_{ij}, so the total escape rate from state i is expressed as the sum of all the rate constants:

$$k_{tot} = \sum_{j} k_{ij} \tag{4.1}$$

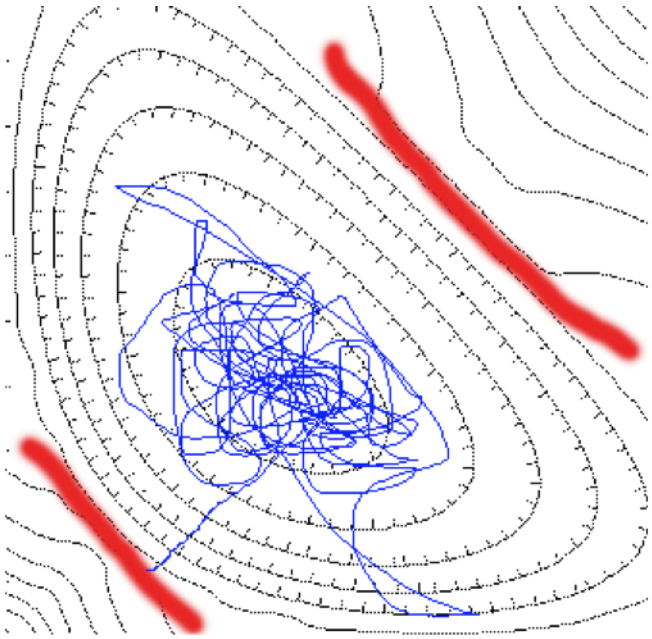

Figure 4.1: Contour plot of the potential energy surface. The blue line maps the random vibrational states experienced by the system as it moves about the energy well until it finds a successful path of escape across an energy barrier, depicted by the red lines, and into an adjacent energy well, moving the entire system to a new energy state.

Equivalently, the transition probability of these rates is defined as [33]:

$$p_{ij} = \frac{k_{ij}}{k_{TOT}} \rightarrow \sum_{j} p_{ij} = 1 \tag{4.2}$$

For each pathway, the escape time distribution from state i to state j is

given by:

$$p_{ij}(t) = k_{ij} \times e^{-k_{ij}t} \tag{4.3}$$

From this probability distribution an exponentially distributed time, t_j, is drawn for each possible escape pathway j. Of course, only one escape pathway can be chosen, so the pathway that corresponds to j_{min} with the smallest t_j is chosen and all other pathways are discarded [32]. The clock is advanced by the time t_{jmin} and the overall system is moved to state j_{min}. It is important to note that the pathway chosen does not always move the system into its lowest energy state. From here the process is repeated until the desired number of steps has been completed. While the process described above is perfectly valid, it is less than ideally efficient due to the programs design, which requires drawing random numbers for each possible escape pathway.

The kMC algorithm is similar to the process described above but more efficient, as it eliminates the need to draw multiple random number distributions to select a pathway. To begin, kMC places the system in some initial configuration state i surrounded by M possible adjacent escape pathways. Each of these pathways are assigned unique lengths directly proportional to their rate constant k_{ij}. Next, kMC will piece together each line segment, such that the total length is given by k_{TOT}. Then a random number r on the interval (0,1) is generated and multiplied by k_{TOT}. Thus we can walk along the line segment of k_{TOT} until we reach the pathway that corresponds to the position $r * k_{TOT}$. This is the pathway that the system will follow. Notice that the

probability of selecting a single pathway is directly proportional to the pathways corresponding rate constant. Figure 4.2 gives a pictorial representation of this process.

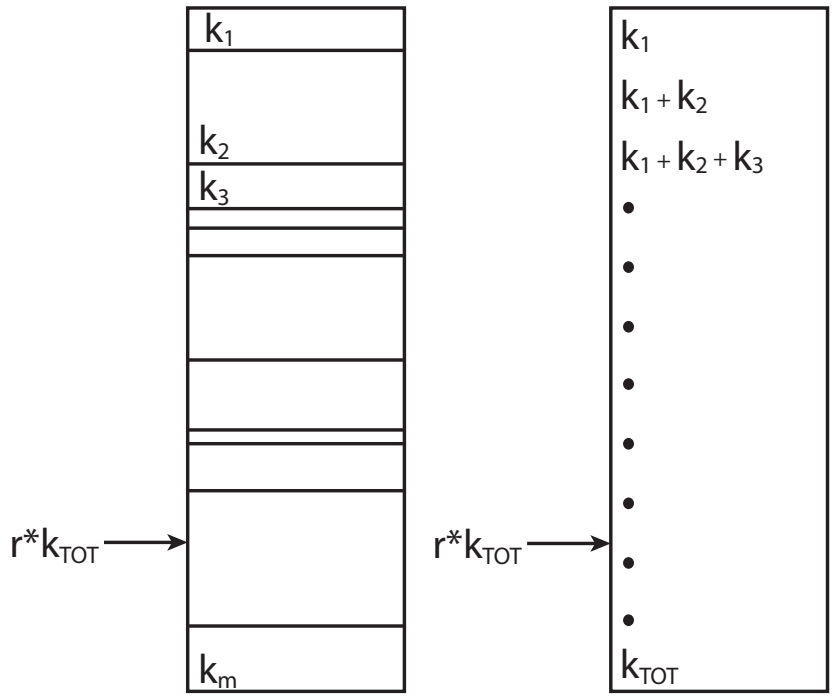

Figure 4.2: Schematic representation of the kMC procedure. Rate constants, depicted as boxes with length proportional to the pathway rate constant are aligned end to end. A random number r is generated between (0,1) and multiplied by k_{TOT}, which corresponds to one box that the system will be advanced to. The image on the right represents a computer code that will compare $r \times k_{TOT}$ to an array of partial sums.

To advance the clock a randomly distributed time is drawn:

$$t_{draw} = -\frac{1}{k} ln(r) \tag{4.4}$$

For this simulation we assume a first order reaction with rate constant k. The escape rate used takes the form of a Poisson process in which specified events occur during a time period from 0 to t. Thus the Poisson process can be thought of as a continuous time Markov chain, where the probability of any future behavior is not dependent on past behavior [34]. With the time t_{draw} the clock is advanced, the list of pathways and rate constants is updated, and the procedure can begin again.

4.2 Graph Theory Methods

The binding and transition state energies for a proton moving in $BaZrO_3$ were found in an earlier study by the Gomez Research Group [35] using VASP. The binding site energies were optimized with the conjugate gradient method for four different H-O bonding orientations. Transition states were calculated using the Nudge Elastic Band method followed by climbing Nudge Elastic Band. The physical system was then mapped to a mathematical graph using vertices to denote binding sites and edges to represent transition states between adjacent binding sites.

The notation $(i_1, i_2, \ldots, i_N)$ is used to denote an N-step pathway through the graph, starting at position i_1 and ending at site i_N. The probability of an

N-step pathway is described by:

$$probability = P_{i_1,i_2}(T)P_{i_2,i_3}(T)\dots P_{i_{N-1},i_N}(T) \tag{4.5}$$

where $P_{i_1,i_2}(T)$ is the probability of the proton moving from binding site i_1 to i_2 and so on until binding site i_N is reached. The probability of a pathway is also dependent upon the temperature, T, of the system.

In order to calculate P, first the rate constant k_{ij}, which quantifies the speed of a reaction, must be calculated. The rate constant between each proton binding site is calculated from

$$k_{i\to j}^{HTST}(T) = \frac{\prod_{k=1}^{N_{vib}} v_k^{min}}{\prod_{k=1}^{N_{vib}-1} v_k^{TS}} e^{-\beta E_{i\to j}^{Barrier}} \tag{4.6}$$

where $\beta = \dfrac{1}{k_B T}$ links the rate constant to the Temperature of the system. Then the probability of selecting one pathway is

$$P_{i\to j}(T) = \frac{k_{i\to j}^{HTST}(T)}{\sum_{j=1}^{M_i} k_{i\to j}^{HTST}(T)} \tag{4.7}$$

where M_i is the number of binding sites adjacent to site i and

$$\sum_j P_{i\to j}(T) = 1 \tag{4.8}$$

Once probabilities between adjacent binding sites have been calculated they are assigned additive edge weights

$$w_{i\to j}(T) = -\ln(P_{i\to j}(T)) \tag{4.9}$$

and the weight of an N-step pathway is the weight of all edges

$$\sum_{n=1}^{N} w_{i_n \to i_{n+1}}(T) \tag{4.10}$$

However, when evaluating probabilities with this method, pathways of different length can not be directly compared because the weights for all possible N-step pathways yields 1 for each size pathway [36].

From graph theory methods, high probability proton conduction pathways have been cataloged. The kinetic Monte Carlo method can now be used to select proton conduction pathways through the system.

4.3 Single Step Proton Pathways Through $BaZrO_3$

The kMC program was allowed to run and high probability proton pathways through the cubic perovskite were located. For a proton's pathway to be considered it needed to start at one binding site and terminate in the same position in a neighboring cube. The shortest pathway found consisted of two rotations followed by two transfer step moves. This pathway is denoted by $RRTT$, and is shown in Figure 4.3. For this specific pathway the proton is

projected through the same horizontal plane.

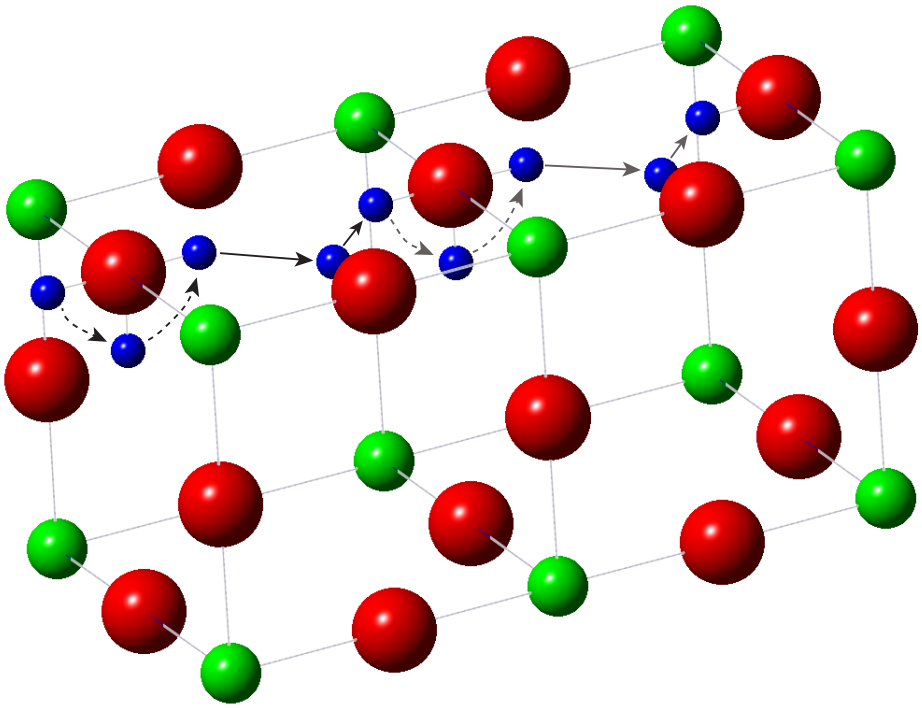

Figure 4.3: A four step pathway through the system, notated as RRTT. The dashed arrows represent rotation about about an oxygen and the solid lines represent transfer between two adjacent oxygen. The lighter grey arrows indicate the beginning of repetition within the pathway

The next shortest periodic pathways within the unit cell are RRTRRT, RTRTRT, and TTRTTR. No five step periodic pathways were found, and pathways longer than six steps were not considered. The six step pathways are shown in Figure 4.4, Figure 4.5 and Figure 4.6.

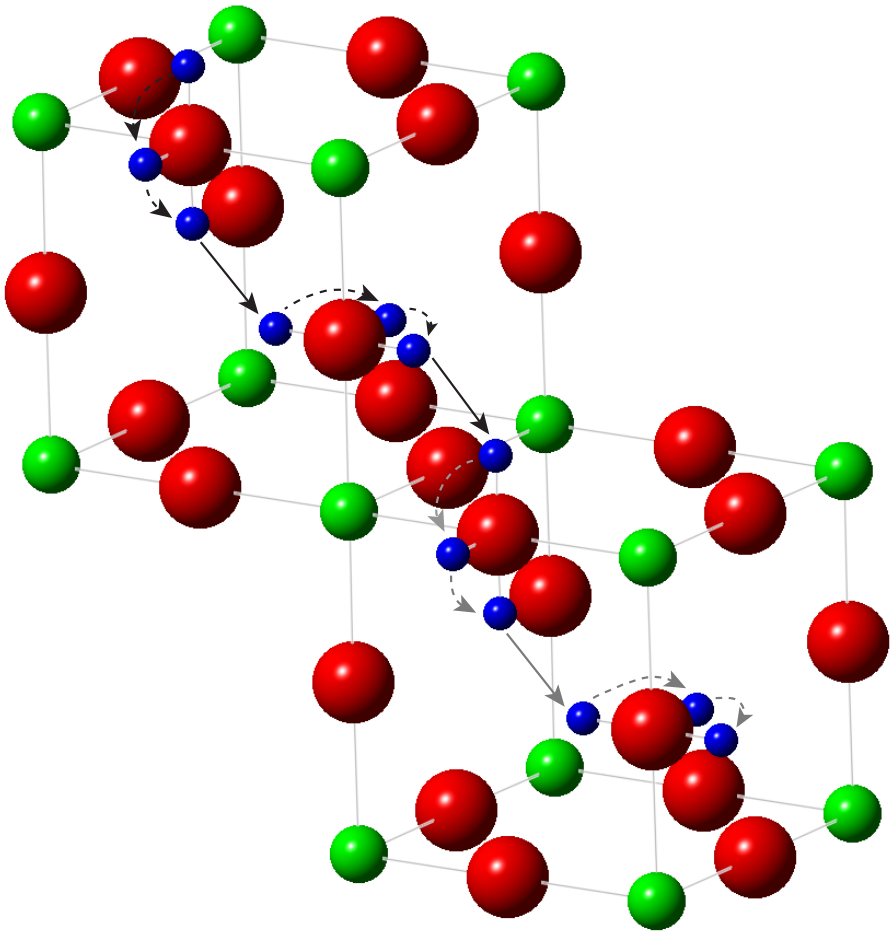

Figure 4.4: A six step pathway through the system, notated as RRTRRT. For details on arrows and coloring see Figure 4.3

The protons trajectory across these pathways can be described as diagonal movement across the unit cell. Geometrically, it would be highly probable that the proton would prefer the most direct pathway across the cube.

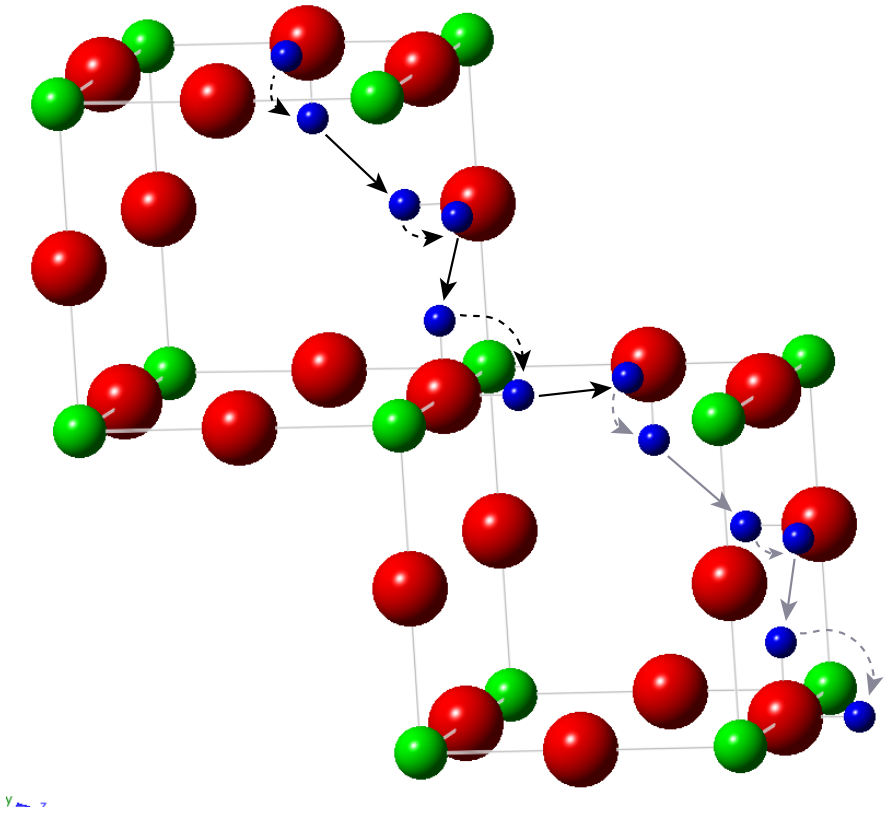

Figure 4.5: A six step pathway through the system, notated as RTRTRT. For details on arrows and coloring see Figure 4.3

These pathways when replicated outward allow the proton to conduct across any length of the system. Therefore the number of six-step minimum energy pathways does not depend on the size of the cubic perovskite [37].

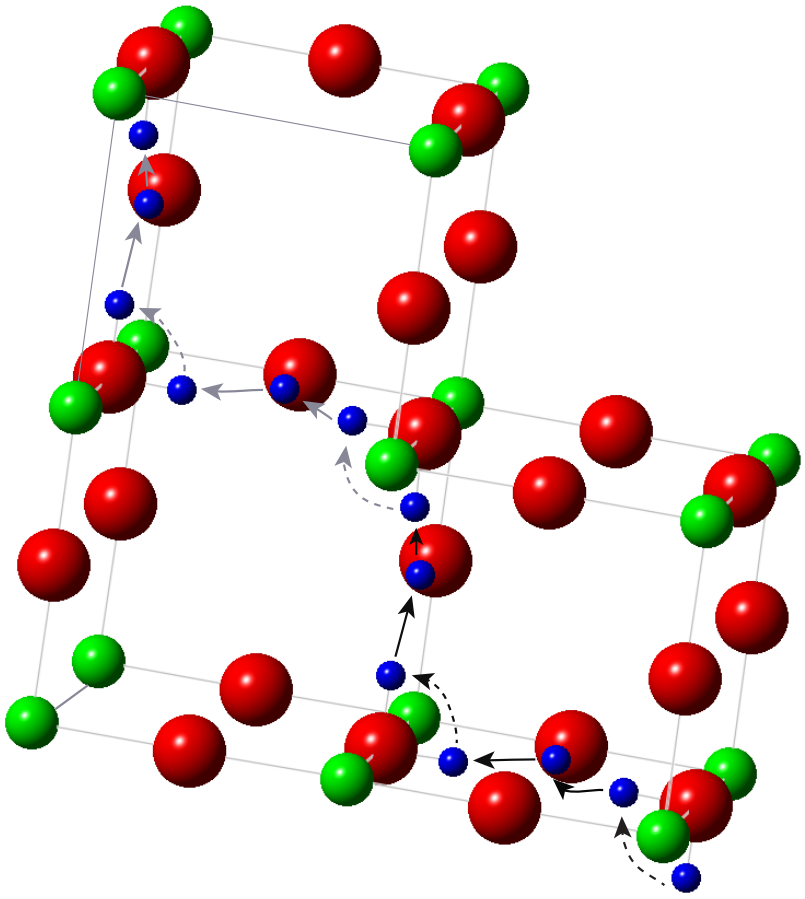

Figure 4.6: A six step pathway through the system, notated as TTRTTR. For details on arrows and coloring see Figure 4.3

4.4 Multiple Step Proton Pathways Through $BaZrO_3$

The previous section looked at the probability of making a single step move away from some initial binding site. Now, an N-step pathway is chosen using the probabilities of all pathways.

The purpose of multi-step moves is meant to decrease the computational time required to locate pathways within the unit cell. To evaluate the running time, pathways of lengths ranging from 1-step to 8-steps were considered. Table 4.1 provides the time required for the kMC program to run.

Table 4.1: Computational Time for N-step KMC

N-Step Pathway Length	Number of Vertices	Run Time Min : Sec
1	2	1:12
2	3	1:09
3	4	1:09
4	5	1:14
5	6	1:18
6	7	1:48
7	8	3:24
8	9	9:59

Overall it appears that the 2-step and 3-step pathways are the fastest to calculate. While the graph theory method is not slowing down computational time, it does not appear to be improving upon it either.

Despite the initial success of our multi-step kinetic Monte Carlo program, several kinks still need to be worked out. The method used to calculate the

amount of time a proton resides in a pathway needs to be adjusted before true analysis of the protons pathway is considered. Currently time steps are calculated based solely on the initial and final positions of the pathway. Intermediate steps are not taken into account, which means that a full analysis of individual steps within the pathway cannot be properly analyzed.

Also, the program has not yet been optimized, and could therefore be performing unneeded or redundant calculations that are increasing the program's overall runtime.

Chapter 5

Future Work

Once the kinetic Monte Carlo program has been adjusted to produce correct time-step calculations, the next step for our research will be to locate high probability proton conduction pathways through a grain boundary. This requires a couple of steps. First, binding and transition states will need to be identified using minimization and Nudge Elastic Band techniques. Additional members in our lab are also working with larger and more realistic grain boundary systems that are currently undergoing minimization. Once pathways through $BaZrO_3$ are located a dopant, either aluminum or yttrium, can be added to the system to study how proton movement is affected when there is an excess charge within the system. These results will help the scientific community to better understand the chemistry of grain boundaries and how proton conduction might be sped up to increase the overall efficiency of fuel cells.

Bibliography

[1] G. Hoogers, *Fuel Cell Technology Handbook*, edited by G. Hoogers (CRC Press, Boca Raton/Florida, 2003), pp 1-5.

[2] A. Varga, *Introduction to Fuel Cell Technology*, (Cambridge/NewYork, 2009), pp1-3.

[3] M. L. Perry, and T. F. Fuller, J. Elect. Soc. **149** S59-S67 (2002).

[4] B. Cook, *An Introduction to Fuel Cells and Hydrogen Technology*, (Canada Heliocentris, Vancouver, BC, 2002), pp. 18.

[5] R. Bove and K. Stahl, Solid State Ionics **8** 372-378 (2005).

[6] EG&G Technical Services, Fuel Cell Handbook Seventh Edition, Morgantown, West Virginia, 2004, pp. 1-10.

[7] H. Ullmann, and N. Trofimenko, Solid State Ionics **119** 1-8 (1999).

[8] M. A. Gomez, M. Chunduru, L. Chigweshe, L. Foster, S. J. Fensin, K. M. Fletcher, L. E. Fernandez, J. Chem. Phys., **132**, 214709 (2010).

[9] F. Giannic, M. Shirpour, A. Longo, A. Martorana, R. Merkle, J. Chem. Mater. **23**, 2994-3002, (2011).

[10] M.A. Gomez, S. Jindal, K.M. Fletcher, L.S. Foster, N. Dufie, A. Addo, D. Valentin, C. Ghenoiu, and A. Hamilton, J. Chem. Phys. **126**, 194701 (2007).

[11] C.Q Tang, L. Liu, X.L. Qian, X. Guo, Y.Q. Sun, K.L. Yao, and K. Cui, Solid State Ionics **4**, 472-476 (1998).

[12] G. Harley, R. Yu, and L. . De Jonghe, Solid State Ionics **178**, 769 (2007).

[13] X. Guo and R. Yuan, Solid State Ionics **80**, 159-166 (1995).

[14] S. Islam, talk at the 2010 Solid State Protonic Conductors 15; H. J. Zhou, Y. B. Mao, and S. S. Wong, Shape control and spectroscopy of crystalline BaZrO3 perovskite particles, J. Mat. Chem. **17**, 1707-1713 (2007).

[15] D.-H Kim, B.-K Kim, and Y.-C Kim, Solid State Ionics (2011), doi:10.1016/j.ssi.2011.05.016

[16] G. Kresse and J. Hafner, Phys. Rev. B **48**, 13115 (1993); G. Kresse and J. Hafner, Phys. Rev. B. **49**, 14251 (1994); G. Kresse and J. Furthmuller, Comput. Mater. Sci. **6**, 15 (1996); G. Kresse and J. Furthmuller, Phys. Rev. B. 54, 11169 (1996).

[17] Adri C. T. van Duin, Siddharth Dasgupta, Francois Lorant, William A. Goddard III, J. Phys. Chem. A **105**, 9396-9409 (2001).

[18] Aktulga, H., Pandit, S., & van Duin, A. (2010). Reactive Molecular Dynamics: Numerical Methods And Algorithmic Techniq by Hasan Metin Aktulga, Shailaja Pandit et al.

[19] A. van Duin, S. Dasgupta, F. Lorant, W.A. Goddard, Phys. Chem. A **105**, 9396 (2001).

[20] A. van Duin, Y. Zeiri, F. Dubnikova, R. Kosloff, W.A. Goddard III, J. Am. Chem. Soc. **127**, 11053 (2005).

[21] K.D. Nielson, A. van Duin, J. Oxgaard, W.Q. Deng, W.A. Goddard, J. Phys. Chem. A **109**, 493 (2005).

[22] V.E. Lamberti, L.D. Foskick, and E.R. Jessup, J. Chem. Ed. **79** 601-606 (2002).

[23] J.D. Evans, and B.L. Holian, J. Chem. Phys. **83**, 4069 (1985).

[24] C.C. Huang, A. Chatterji, G. Sutmann, G. Gompper, and R.G. Winkler, J. Comp. Phys. **229**, 168-177 (2010).

[25] R. P. Feynman, R. B. Leighton and M. Sands, The Feynman Lectures on Physics, Vol. 1, Addison-Wesley, 1963, Chapter 9 ("Newton's Laws of Dynamics").

[26] M.C. Payne, M.P. Teter, D.C. Allan, T.A. Arias, and J.D. Joannopoulon, Rev. Mod. Phys. **64**, 1070-1072 (1992).

[27] A.M. Glazer, Acta Cryst. B **28**, 3384-3392 (1972).

[28] D. Sheppard, P. Xiao, W. Chemelewski, D.D Johnson, and G. Henkelman, J. Chem. Phys. **136**, 074103 (2012).

[29] G. Henkelman, B.P. Uberuaga, and H. Jonsson, J. Chem Phys. **113**, 9901 (2000).

[30] M.H. Kalos and P.A. Paula, *Kinetic Monte Carlo Methods*, (John Wiley & Sons Ltd, New York, 2001), p1-2.

[31] C.C. Battaile, Comput. Meth. Appl. Mech. Engrg. **197**, 3386-3398 (2008).

[32] A.F. Voter, *Introduction to the Kinetic Monte Carlo Method* Radiation Effects in Solids, edited by K.E. Sickafus and E.A. Kotomin (Springer, NATO Publishing Unit, Dordrecht, The Netherlands, 2005) Volume **235**: 1-23.

[33] T.P. Schulze, J. Comp. Phys. **227**, 2455-2462 (2008).

[34] A. Karlin and H.M. Taylor, *A First Course in Stochastic Processes*, (Academic Press Inc., San Diego, 1975), p.22-26.

[35] M.A. Gomez, M. Chunduru, L. Chigweshe, L. Foster, S.J. Fensin, K.M. Fletcher, and L.E. Fernandez, J. Chem. Phys. **132**, 214709 (2010).

[36] M.A. Gomez, D. Shepardson, L.T. Nguyen, and T. Kehinde, Solid State Ionics, **213**, 8-13 (2012).

[37] Saryu Jindal. Senior thesis. Mount Holyoke College 2006.